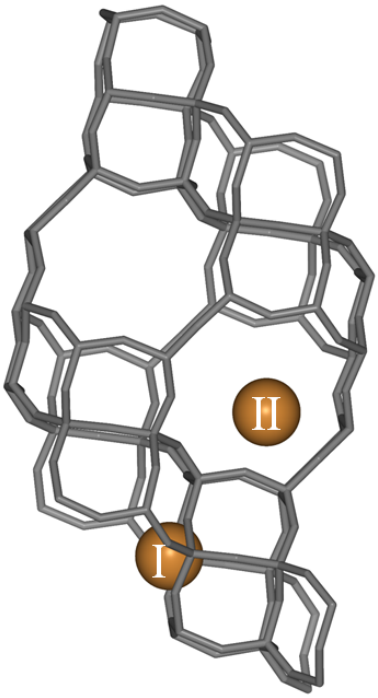

Studying the atomic structure of an electron beam sensitive catalyst

Developing methodologies for studying Cu-SSZ-13 catalyst with high-resolution electron microscopy

Master's thesis in Physics

CARL ANDERSSON

DEPARTMENT OF PHYSICS

CHALMERS UNIVERSITY OF TECHNOLOGY
Gothenburg, Sweden 2021
www.chalmers.se

Master's thesis 2020 - 2021

Studying the atomic structure of an electron beam sensitive catalyst

Developing methodologies for studying Cu-SSZ-13 catalyst with high-resolution electron microscopy

CARL ANDERSSON

CHALMERS
UNIVERSITY OF TECHNOLOGY

Department of Physics
Division of Nano and Biophysics
Eva Olsson Group
Chalmers University of Technology
Gothenburg, Sweden 2021

Studying the atomic structure of an electron beam sensitive catalyst
Developing methodologies for studying Cu-SSZ-13 catalyst with high-resolution electron microscopy
CARL ANDERSSON

© CARL ANDERSSON, 2021.

Supervisor: Eva Olsson, Department of Physics
Examiner: Eva Olsson, Department of Physics

Master's Thesis 2021
Department of Physics
Division of Nano and Biophysics
Eva Olsson Group
Chalmers University of Technology
SE-412 96 Gothenburg
Telephone +46 31 772 1000

Cover: Two Cu active sites illustrated inside the zeolite framework of Cu-SSZ-13.

Typeset in LaTeX
Gothenburg, Sweden 2021

Abstract

This work concerns catalysts and the optimisation of atomic structure to increase the catalytic efficiency and lifetime of said systems. Catalysts are used in many different applications, for example vehicles, chemical synthesis, biological reactions and food processing. The increasingly stringent regulations regarding vehicular emissions have brought about an intense research in automotive catalyst systems during the last decades. In this work we focus on the zeolite system Cu-SSZ-13, one of the leading candidates for state-of-the-art heavy-duty automotive catalyst systems, and developing a methodology for studying it with atomic resolution scanning transmission electron microscopy (STEM) imaging. Proper specimen preparation is one of the most important factors in order to achieve high-resolution. A substantial part of this work therefore concerns the study how to optimally prepare SSZ-13 samples for high-resolution imaging. Specifically, we try to find methods for imaging and specimen preparation that limit electron beam damage of Cu-SSZ-13. We present a protocol for specimen preparation of SSZ-13 that also includes information about different means of controlling the degree of sample hydration and its effect upon the sensitivity to electron beam damage. Beam damage effects and underlying mechanisms are discussed as well. We also present results from simulations of atomic resolution images of Cu-SSZ-13, which in turn can be used to support experimental results of future works.

Keywords: SCR, Zeolite, Cu-SSZ-13, Electron microscopy, High resolution, HAADF STEM, Specimen preparation, Simulation.

Acknowledgements

I would like to express my sincerest gratitude to my supervisor and examiner Prof. Eva Olsson for all your help, guidance and outstanding support throughout my project, especially for the many extra hours spent discussing my texts and writings.

I would also like to give a huge thanks to Mike Schmithorst and Prof. Brad Chmelka at UCSB for the collaboration that led to this project, for providing us with our experimental samples, and for nice discussions and support regarding the material.

I would like to thank all members of the Eva Olsson Group for a lot of support during the year. Special thanks go to Dr. Shun Kondo for many hours spent at the microscope, Dr. Andrew Yankovich and Dr. Lunjie Zeng for a lot of help and nice conversations and Gustav Persson for our arduous but educational attempt to apply graphene to our microscopy samples.

Most of this work has been carried out within CMAL (Chalmers Materials Analysis Laboratory), and I would like to thank you all for your advice and help with the instruments. Especially a big thanks to Dr. Ludvig de Knoop and Dr. Stefan Gustafsson for always helping me out at the microscopes.

Finally, I would like to say thanks to Yifei Zhang for help with operating the glove box used in this project, Assoc. Prof. Anders Hellman for the help with constructing a simulation model cell, and Naveen Shetty and Assoc. Prof. Samuel Lara Avila for helping us out in the Chalmers Nanofabrication Laboratory.

Carl Andersson, Gothenburg, June 2021

Contents

List of Figures

List of Tables

1

Introduction

During the last decade rigorous emission rules, such as the Euro VI or US 2010, have been established to reduce vehicle emissions. These rules set limits for many of the harmful compounds contained in automotive exhausts. Today most commercial heavy-duty vehicles rely on urea-based Selective Catalytic Reduction (SCR) to convert harmful nitrogen oxides (NOx) into nitrogen N_2 and water [1]–[4]. For future applications, increasingly stringent legislations demand even more effective catalysts.

One of the of the main problems to overcome for new SCR techniques is a broader operating window for temperature. For example to increase efficiency during cold starts and enhanced high-temperature stability [1], [4]. Among the leading candidate materials for state-of-the-art SCR systems are transition metal infused zeolites [1], [5], [6]. Zeolites are microporous, aluminosilicate minerals which both exist as natural minerals and synthesized versions. The zeolite SSZ-13 (infused with transition metals such as Pd or Cu) is one of the more promising materials to expand the temperature operating window of SCR catalysts due to its high activity and thermal durability [1]–[3]. The copper infused SSZ-13 (Cu-SSZ-13) is highly active in a broad temperature range and with a reduced amount of undesired by-products. This suggests that Cu-SSZ-13 is an excellent candidate for use in practical SCR applications [1], [2], [7].

As with all catalysts, there is a close relationship between the atomic structure, composition and the catalytic activity of the material. The nanoscale also introduces additional mechanisms caused by quantum effects becoming evident. In the case of SSZ-13 the precise positions of the Cu or Pd cations within the pores of the zeolite are also of paramount importance to the lifetime and stability of the catalyst [8].

Bulk measurements that produce an averaged picture of the dispersion have been performed before in the literature [8]–[15]. Site-specific characterization with nanoscale resolution, such as electron microscopy, are however generally missing. The aim of this work was to study methods for imaging and specimen preparation that limit electron beam damage to a degree that enables atomic resolution imaging of Cu-SSZ-13. This project is a collaboration between University of California, Santa Barbara and Chalmers University of Technology.

2

Background

In this chapter, the role of SSZ-13 in automotive catalytic converters will be discussed. In the first section, the Selective Catalytic Reduction (SCR) and its part in the aftertreatment system of a heavy-duty vehicle will be described. In section 2.2, important findings relating to the active sites in SSZ-13 will be presented in order to understand their properties.

2.1 Selective Catalytic Reduction

The key, simplified SCR catalyst reactions for reduction of nitrogen oxides (NO_x) are

$$4NH_3 + 4NO + O_2 \rightarrow 4N_2 + 6H_2O \tag{2.1}$$

$$2NH_3 + NO + NO_2 \rightarrow 2N_2 + 3H_2O. \tag{2.2}$$

The first reaction, eq. (2.1), uses NO and is called the "standard" SCR reaction [1], [4]. The second reaction, eq. (2.2), is called the "fast" SCR reaction and uses equimolar amounts of NO and NO_2 [16]. This is the preferred reaction since it leads to a higher NO_x reduction rate than the standard reaction [1], [4], [16].

A typical, modern aftertreatment system for heavy duty diesel vehicles includes a diesel oxidation catalyst (DOC), a diesel particulate filter (DPF) and the SCR, all mounted close together [4]. The DOC has two primary roles within the catalyst: to oxidize hydrocarbons and CO as well as to oxidize NO to NO_2. A higher amount of NO_2 compared to NO is desired to promote the fast SCR reaction of (2.2) [4]. The role of the DPF is to continuously filter out soot from the exhaust stream to reduce the amount of particulate matter.

Three of the main materials used in the SCR are vanadia, copper infused zeolites and iron infused zeolites [1], [4], [17]. Vanadia based catalysts are the cheapest of the three but are sensitive to high temperatures, making these catalysts difficult to use together with a DPF [4]. Iron zeolites have the best high temperature performance but show reduced efficiency at lower temperatures common to normal diesel engine operation [4], [17]. The efficiency at lower temperatures is important in reducing No_x emissions during, for example, cold starts and stop-and-go urban driving conditions [1], [4]. In the lower temperature region, Cu zeolites have shown much greater promise than Fe zeolites. This work focuses on Cu zeolites due to their higher potential at lower temperatures [1], [7], [17].

2.1.1 Degradation processes for zeolites

A zeolite's structure will eventually collapse when it is heated to high temperatures. The inevitable existence of water within the exhaust stream accelerates this process, which is called hydrothermal ageing [17]. Two of the most important degrading processes due to hydrothermal ageing in Cu zeolites are dealumination and

agglomeration of isolated Cu ions into CuO clusters [18]. During dealumination, Al atoms in the zeolite are detached from the framework and create defect sites at the associated locations [17].

Under normal operating conditions the temperature is too low for hydrothermal ageing to occur [4]. The DPF, however, requires periodic regeneration events where trapped particulate matter are burnt off [17]. The temperature of the whole system rises drastically during the burn off.

Sulfur from the exhaust can also readily react with the Cu in the material, forming $CuSO_4^-$ complexes that degrade the catalytic activity [17]. These complexes must also be burnt off, further showing the need for the periodic regeneration events [17].

All taken together, the current design of SCR systems results in the hydrothermal stability of a material being a very important property which needs to be taken into account when developing zeolite materials for SCR.

2.2 SSZ-13 Chabazite

During the last decade, Cu infused zeolites have attracted significant attention for their use in SCR catalysts. Cu or Fe exchanged zeolites have become two of the main NO_x abatement techniques for diesel engine exhausts [4]. In 2007 Cavatio et al. demonstrated the high performance of Cu doped zeolites as NH_3-SCR catalysts [7] in comparison with the two other common SCR materials, vanadia and Fe zeolite catalysts. They showed that Cu doped zeolites are stable over a broader temperature range as well as more active than other investigated materials. The Cu doped zeolites also show higher activity at lower temperatures compared to the other two materials. This is an important factor when considering the cold-start problem for automotive vehicles.

In 2010 some of the first open literature investigations demonstrating the high performance of Cu-SSZ-13 were published [2], [19]. Within the limitations of these studies, Cu-SSZ-13 shows a NO_x conversion rate close to 100 % during a temperature range between $\sim$ 200 °C - 400 °C and still maintains high activity after a hydrothermal ageing process. These properties make Cu-SSZ-13 highly interesting in the field of SCR catalysts.

2.2.1 Cu-SSZ-13 structure

SSZ-13 is a synthesized aluminosilicate zeolite with the same CHA-structure as naturally occurring chabazite. It was first discovered by Zones et al. in 1985 [20]. The CHA framework adopts the $R\bar{3}m$ space group and has a small pore structure where the largest pores are found within the eight-membered rings and have a diameter of $\sim$3.8 Å [21]. The SSZ-13 framework consists of the elements Si, Al and O. Cu is added to the framework during synthesis. In this work, Cu-SSZ-13 with Si/Al ratio of 10:1 and a Cu content corresponding to 3.3 weight percent (wt%) was used.

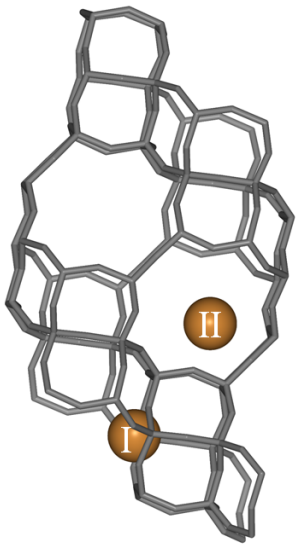

Figure 2.1: The two proposed Cu cation positions within the SSZ-13 CHA-framework: the 6MR (I) and the 8MR (II). The Cu cations are enlarged for visualization.

2.2.2 Active species and their locations in dehydrated SSZ-13

With all catalysts there is a close correlation between the spatial structure and the catalytic activity of the material. This relationship can be quite difficult to unravel on the molecular scale and for the SCR reaction it is not yet understood for Cu-SSZ-13 [22].

However, many different studies during the last ten year have singled out two different Cu cations as the active species for this catalyst: Cu^{2+} and $[Cu(OH)]^{+}$ [8], [9], [11], [13]–[15], [23]–[26]. In the silicon framework of zeolites, the aluminum atom introduces a charge imbalance due to its three valence charges compared to the four of silicon [17]. Both of the above mentioned Cu cations have in common that their positive charge can compensate for this imbalance. It should be noted that Cu^{2+} needs to be balanced by two nearby framework negative charges (Fig. 2.2a) while $[Cu(OH)]^{+}$ needs to be balanced by only one (Fig. 2.2b) [18], [27]. The catalytic activity of the two Cu species is similar, but Cu^{2+} is more stable than $[Cu(OH)]^{+}$ with respect to hydrothermal ageing [8], [28].

In the following sections the different species are further described.

2.2.2.1 The Cu^{2+} species

The evidence of the catalytic activity of the Cu^{2+} ion was first provided in 2010 [14]. The preferred position of the ion in the six-member ring (6MR), see Fig. 2.2a and position I in Fig. 2.1, was identified by using both Rietveld refinement of X-Ray diffraction (XRD) data [14] and X-ray absorption fine structure (XAFS) [15]. Two years later it was confirmed by synchotron based XAFS and XRD that Cu^{2+} is active in the catalytic SCR reaction [23].

(a) Cu within the 6MR

(b) Cu within the 8MR

Figure 2.2: Example of configurations for the two proposed Cu cation positions within SSZ-13. The color coding is as following: Si in light brown, O in red, Al in grey and Cu in brown. Note that there are two Al atoms stabilizing the Cu in (a) and only one in (b).

Paolucci et al. used density-functional theory (DFT) a few years later to compare the free energy of Cu near 2 Al (Fig. 2.2a) with Cu near 1 Al (Fig. 2.2a) [24]. From this result it has been concluded that Cu^{2+} within the 6MR is the most energetically favorable position of the two [8], [18], [27].

2.2.2.2 The $[Cu(OH)]^+$ species

The existence of another active site for Cu in addition to Cu^{2+} in the 6MR was first proposed by Kwak et al. on the basis of H_2 temperature-programmed reduction (H_2-TPR) and Fourier transform infrared (FTIR) spectroscopy [11]. Later an additional Cu species within the eight-member ring (8MR) was found by Rietveld refinement (position II in Fig. 2.1) [26]. DFT was used to suggest that this unknown form of Cu could be $[Cu(OH)]^+$ balanced by a single Al atom (see Fig. 2.2b) [26]. The actual existence of $[Cu(OH)]^+$ within the zeolite was shown using IR spectroscopy [12] and electron paramagnetic resonance (EPR) [13].

2.2.3 Sensitivity of the active species

As stated above, two of the main destructive processes that deteriorate catalytic activity and which are induced by hydrothermal ageing are zeolite dealumination and agglomeration of isolated Cu ions into CuO complexes [17], [18].

Kharas et al. studied the catalytic deactivation as well as the crystal structure of a Cu-ZSM-5 zeolite similar to Cu-SSZ-13 [10]. Using XRD and extended XAFS analysis they discovered a loss of both micropore volume and crystallinity as well as an increase of CuO species during deactivation of the catalyst. FTIR spectroscopy showed that the catalytic deactivation of Cu-SSZ-13 became more severe with increasing Cu/Al ratio of the material [9].

On the basis of H_2-TPR, EPR and IR spectroscopy results this deactivation, in line with the result of Kharas et al., was related to the formation of CuO species (CuO_x). A greater affinity for Cu located outside of the 6MR (for example $[Cu(OH)]^+$ in the 8MR) to convert to CuO_x during hydrothermal ageing was also found [9].

Song et al. continued to study this phenomenon in 2017, with a focus on the effect of hydrothermal ageing on two specific active sites, i.e. Cu^{2+} in the 6MR and $[CuOH]^+$ in the 8MR [8]. Using mainly nuclear magnetic resonance (NMR), EPR and IR spectroscopy together with DFT they showed a number of properties regarding the degradation processes in SSZ-13. First of all they proposed that dealumination is not a primary cause of damage during hydrothermal ageing. They also showed, in line with the findings stated above, the difference in stability between the two active species where the Cu^{2+} is more stable. It is primarily $[Cu(OH)]^+$ in the 8MR that converts to CuO_x during ageing [8]. Finally they proposed that the movement of these CuO_x clusters within the zeolite are responsible for the degradation of the framework [8].

2.2.4 Directing the active sites

Increasing the ratio of Al compared to Si in the zeolite framework also increases the ratio of Cu^{2+} in relation to $[Cu(OH)]^+$ [8], [24]. This effect has been linked to the increased likelihood of finding double Al atoms in the 6MR (see Fig. 2.2a) at higher Al loadings [8], [24], [29]. With this in mind, it has been suggested that by controlling the Al loading, one can also control the distribution of active species in the material, and thus also control the hydrothermal stability. This effect was studied in a recent article by Di Iorio et al., where different structure-directing agents were used to promote the formation of 6MR or 8MR paired Al arrangements during the zeolite synthesis [29].

In summary, the exact positions of the Cu cations is crucial for the understanding of the effect of different synthesis procedures on the catalytic activity. The different methods used in previous studies (NMR, XRD etc.) to study the positions of the cations are all to some degree dependent on either a pre-existing model of the system or requires averaging over large ensembles. A direct observation of the cations within the structure, such as by scanning transmission electron microscopy (STEM), would be a welcome complement to the above mentioned methods. To the best of our knowledge, no STEM imaging of Cu ions within the SSZ-13 framework has yet been performed.

3

Experimental methods

In this chapter, the experimental methods and our specimen preparation process will be described. We will introduce the concepts behind Scanning Transmission Electron Microscopy and discuss different types of signals and detectors, microscope resolution as well as a method to monitor the orientation of the specimen inside the microscope. We will also address beam-specimen interactions, with a focus on electron beam damage. We describe two methods we have used for specimen preparation, one well-proven from the literature and one developed in-house. Finally, we briefly discuss how to avoid moisture from absorbing into the sample, something which potentially could complicate the imaging process.

3.1 Scanning Transmission Electron Microscopy

In electron microscopy a beam of high energy electrons, contrary to visible light in conventional microscopy, is used as illumination. These electrons interact with the specimen and the resulting signals can provide both high resolution images and spectroscopic information.

A specific technique within electron microscopy is scanning transmission electron microscopy (STEM). Here the incident electron beam is focused to create a small probe on the specimen. The probe is then scanned across the specimen and detectors above and beneath the sample collect the signals for imaging and spectroscopy.

3.1.1 Types of scattering

When the incident electrons travel through the specimen there are three different scattering scenarios:

No interaction Electrons that pass through the sample without interaction are called the ”direct” electrons. These electrons experience no change of either direction or energy as they pass through the sample.

Inelastic scattering Inelastically scattered electrons have lost some amount of their initial energy to the scattering process. This type of scattering generates a whole range of signals which can be measured for information about the chemistry of the specimen. Examples of signals arising from inelastic scattering are characteristic X-rays as well as electrons for electron energy loss spectroscopy (EELS).

Elastic scattering Elastically scattered electrons lose a negligible amount of energy during the scattering process. One of the primary processes that induces this kind of scattering is when the incident electrons interact with the positive nucleus of an atom in the sample. This interaction can be described as Rutherford scattering

and the resulting electrons scatter through large angles [30]. The cross section for Rutherford scattering is strongly related to the atomic number, Z, density, ρ, and thickness, t, of the sample [30].

3.1.2 STEM detectors

The STEM detectors consist of concentric rings that each capture electrons scattered within a specific range of angles. Figure 3.1 shows a schematic overview of the convergent electron beam hitting the specimen and the resulting signals. The detectors are generally split into three different types:

Bright field A bright field detector (BF) collects the direct electrons or those with a very small scattering angle. The contrast in the images formed by this detector is heavily influenced by interference between transmitted coherent electrons [31]. This fact can be both useful and detrimental depending on the goal of the microscopy.

High angle annular dark-field For electrons scattered at high angles, a high-angle annular dark-field (HAADF) detector is used. Most of the electrons captured by the HAADF detector have been Rutherford scattered. This scattering is strongly related to the chemical composition (atomic number) and thickness of the specimen. HAADF imaging has also been shown to generally be due to incoherent scattering [31]. This minimises the effect of interference between the electrons scattered from different atoms [32], [33]. All together, this leads to a more straightforward interpretation of the images in terms of atom types and their positions [32], [33], especially in comparison to results from the BF detectors where the image contrast is more dependent upon interference. For example, the intensity of HAADF-images (assuming uniform thickness) can be shown to be proportional to $\approx Z^2$, where Z is the atomic number of the material [34].

Annular dark-field An annular dark-field (ADF) detector excludes the electrons close to the optical axis and acts as a middle ground between the BF and the HAADF, both in a literal sense and in terms of image formation. The detector itself is placed between the BF and HAADF. The contrast in the ADF image results from a non-trivial blend of coherent and incoherent scattering - the exact mix being highly dependent on the limiting collection angles of the detector [31].

In addition, the thickness of the sample may also induce a contrast reversal effects, further complicating the interpretation [31].

3.1.3 Resolution and aberrations

To approximate the theoretical resolution differences between conventional optical microscopy and electron microscopy we can use the Rayleigh criterion ([30], [35])

$$d \approx 0.61 \frac{\lambda}{\sin(\beta)}. \tag{3.1}$$

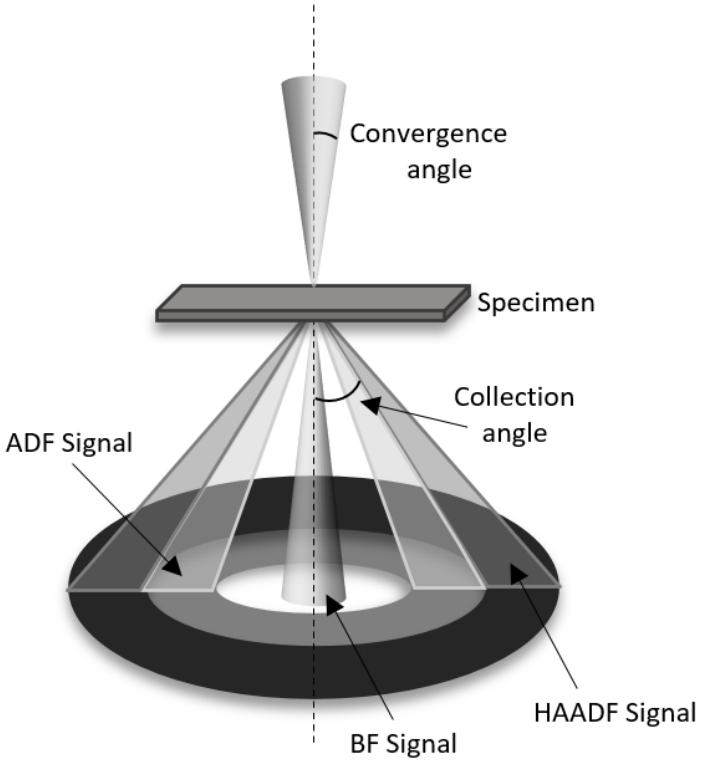

Figure 3.1: Schematic drawing showing the principle of STEM. A convergent electron beam hits the sample and generates signals to the three concentric detectors. The angles are exaggerated for clearer illustration. BF: bright-field, ADF: annular dark-field, HAADF: high-angle annular dark-field.

In (3.1) d is the smallest diameter of a disc that a lens can focus a beam into. Thereby d also describes the limit of resolution for the system. The parameter β in (3.1) is the collection semi-angle of the lens in the system.

If we use (3.1) on a wavelength located in the middle of the visible spectrum (green light with $\lambda \approx 550\,\text{nm}$), we get an approximate maximum resolution of 300 nm for a conventional microscope. The electrons in a 300 keV TEM instead have a wavelength of $\lambda \approx 2\,\text{pm}$ [30]. Assuming a convergence semi-angle of 25 mrad, equation (3.1) yields a resolution of about 0.8 Å. Considering the fact that the dimension of an atom is on the order of 1 Å, it is evident that high resolution electron microscopy enables the study of individual atoms and beyond.

In reality however, we can't readily achieve this resolution due to imperfections in the magnetic lenses. These imperfections give rise to different aberrations that limit the factual resolution by focusing a beam of electrons into a disc instead of a perfect point. Examples of aberrations are astigmatism, spherical aberration, and chromatic aberration.

Astigmatism results from the magnetic field of the lenses not being perfectly symmetrical [30]. This causes an elongation of the focused spot into an ellipsoidal disc. With respect to the other aberrations, astigmatism can be comparatively easily corrected for by using stigmators within the microscope. These components introduces a compensating magnetic field to balance the astigmatism [30].

The chromatic aberration is due to the magnetic lenses more strongly affecting electrons with longer wavelengths compared to those with shorter wavelength [30]. The effect is evident both for the illumination system and the TEM imaging system. A monochromator reduces the effect in the illumination system but has the disadvantage of reducing the probe current.

Another imperfection of the lenses results in electrons being bent more strongly the further off the optical axis they are [30]. This is the effect of spherical aberration and can be remedied by using a small convergence angle (see Fig. 3.1). The spherical aberration is evident in both TEM and STEM and the introduction of a spherical aberration corrector can compensate for this effect in both operation modes [36].

3.1.4 Electron beam damage

The interaction between the high energy electrons and the sample is the process responsible for the image formation. However, the interaction can also have a detrimental effect: specimen damage. One way to categorize the induced damage is by the mechanism responsible for it. Common categories include knock-on damage, radiolysis, electrostatic charging and heating [37]. The process responsible for each type of damage often involves a myriad of complex interactions and consequently the categories sometimes overlap. In the following section we examine each damage type in further detail.

Knock-on damage A fraction of the incident electrons passes close enough to the nucleus of atoms in the sample to be Rutherford scattered. This elastic scattering transfers an amount of energy

$$E = E_{max}(E_0)\sin^2(\theta/2) \tag{3.2}$$

to the nucleus itself. In (3.2) θ is the scattering angle and E_{max} is the energy loss for 180° scattering [37], [38]. E_{max} in turn depends on the energy of the incident electrons E_0. Damage may occur if the transferred energy is greater than the critical displacement energy E_c. This critical energy is lower for atoms close to a surface in the specimen [37]. Lowering the incident energy E_0 results in a lower E_{max} and thus this type of damage can be reduced by choosing a lower acceleration voltage [37].

Radiolysis Radiolysis is an inelastic process where some amount of energy is transferred from the incident electrons to the atoms in the sample. The amount of energy can be anywhere between a few eV and hundreds of eV depending on how strongly the electrons are bound to the their specific atoms in the sample [37]. If the induced excitations last long enough they may result in a permanent breakage of chemical bonds and a displacement of atoms or molecules. This type of damage is rarely a problem in metal-like materials since the excited electrons quickly relax back before damage occurs [37].

The general consensus is that radiolysis is dependent on the accumulated dose of electrons rather than on the acceleration voltage, which is the case of knock-on damage [30], [37], [38].

Electrostatic charging A poorly conducting specimen may accumulate enough charge to induce a high electric field in a region around the beam. If the magnitude of the field is large enough the electrostatic forces can induce a breakdown of the sample [37], [38]. Electrostatic charging involves both inelastic (secondary and Auger electrons) and elastic (backscattered) processes [37].

Heating Not all the energy transferred by inelastic scattering ends up as radiolysis excitations. In fact, most of the energy transferred to the specimen turns into heat [38]. Despite this, the actual temperature rise is generally low [38]. This means that specimen damage due to heat is rarely a problem – the exception being materials with poor thermal conductivity and a low threshold for temperature degradation [37].

3.1.4.1 Dominant damage mechanisms for zeolites

Even though all of the above damage mechanisms, to some degree, occur concurrently to a material in the electron microscope, one or a few of them are often dominant. For zeolites, radiolysis is often raised as the dominant damage mechanism throughout the literature [39]–[44]. Radiolysis is however a concept that includes many mechanisms. For zeolites, there are especially two aspects that have been found to impact the sensitivity to electron beam damage. One is the Si/Al ratio, where the stability of the zeolites increases with the Si content [40], [41], [43]–[47]. Another factor is related to water, where the rate of damage has been linked to the degree of hydration [43], [47]–[49]. A mechanism for this effect has been proposed in which water molecules interact with the electron beam and acidic species (such as OH^- and H^+) are formed [47]. These reactive species then destroy the zeolite framework.

3.1.5 Tilting to zone axis

Since a HAADF-STEM image in essence is a 2D projection of several atoms, it is important to tilt the sample to an orientation where many atoms line up in order to get an interpretable image (see for example Fig. 3.6 in section 3.2.3). Kikuchi lines can be very helpful to keep track of the orientation of a crystalline sample in the microscope. To describe what these lines are and how they can be used, we must look closer at the electron scattering within the specimen.

3.1.5.1 Kikuchi line basics

If the specimen is thick enough, we will at any given time have a large number of electrons travelling through the specimen in (mostly) random directions due to incoherent scattering. Some of these incoherently scattered electrons will hit crystal planes at the Bragg angle θ_B, defined by

$$n\lambda = 2d\sin(\theta_B), \tag{3.3}$$

resulting in constructive interference and a contrast on the viewing screen of the microscope [30]. In (3.3), n is the diffraction order, λ is the wavelength of the electrons and d is the interplanar distance of the crystal planes. Since the diffusively scattered electrons come upon the planes from all directions, the Bragg condition is fulfilled at an angle θ_B defining a cone at the plane. These cones of constructively interfering electrons are called Kossel cones [30]. The Bragg angle is very small for electrons (due to their small De Broglie wavelength) which results in the cone angle (between the cone and the plane) being very small and the cone surface being almost parallel to the crystal planes they scattered from. When the crystal is oriented so that the corresponding crystal planes are in close proximity of being parallel to the incident electron beam, the Kossel cones appear as (slightly bent) lines in the diffraction pattern on the viewing screen (see Fig. 3.2) [30]. These lines are called Kikuchi lines.

3.1.5.2 Tilting using Kikuchi lines

If the crystal is tilted, the lines on the viewing screen will move accordingly. Using this we can use the lines as "map" of the reciprocal space where a zone-axis (high-symmetry orientations where we have Bragg diffraction from many planes simultaneously) show up as intersections between many lines [30]. The Kikuchi pattern of each zone-axis is uniquely tied to its diffraction symmetry and can thus be used as "pin-points" on the Kikuchi map to keep track of the orientation of the specimen (see Fig. 3.3) [30].

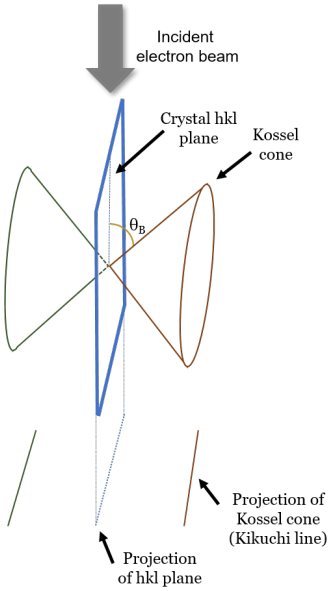

Figure 3.2: Even though the incident electron beam does not fall upon the crystal plane at the Bragg angle, many of the incoherently scattered electrons do. These come from all directions and thus we have constructive interference in a cone around the crystal planes. Where the Kossel cones intersect the focal plane, they show up as nearly straight lines called Kikuchi lines in the diffraction pattern on the viewing screen. Figure adapted from [30].

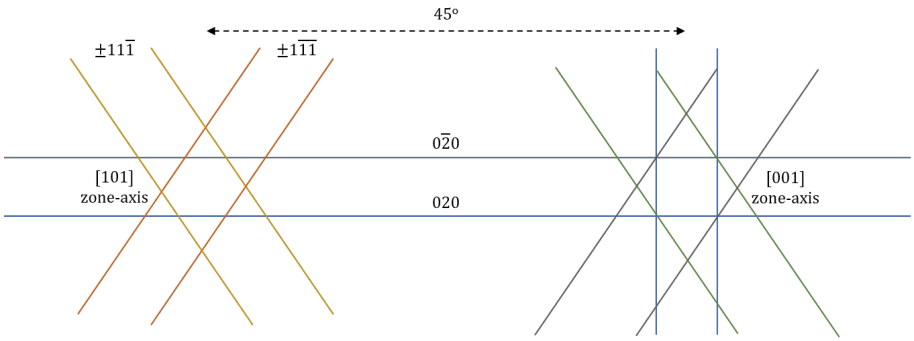

Figure 3.3: Example of Kikuchi map linking the [101] zone-axis to the [001] zone axis. The distance between the two axes on the viewing screen corresponds to the 45° difference between the axes in real space. The axis and its corresponding Kikuchi lines are related by Weiss zone law: hU+kV+lW= 0, where [UKW] describes the zone-axis index and hkl describes the crystal plane index. Figure adapted from [30].

3.2 Simulations

To verify any experimental observation, it is essential to compare the results with known theory and calculations. In this chapter, simulated high-resolution images from two different software are presented and discussed. Experimental high-resolution images can then be compared to these image simulations to further validate any conclusions. Two different software, QSTEM and µSTEM, were used for the simulations in order to cross-check the results from the simulations.

3.2.1 Simulation parameters

The simulations were carried out at an acceleration voltage of 300 kV and a beam convergence angle of 25 mrad (see Fig. 3.1). The supercell thickness was set to 200 nm since this mostly represents the size of the preferred experimental crystals (see section 4.1 for a further discussion). Three different detectors, with collection angles set to representative settings of experimental parameters, were used for each simulation. These corresponded to a BF detector (collection angle 0-2 mrad, see Fig. 3.1), an ABF detector (collection angle 10-20 mrad) and a HAADF detector (collection angle 70-220 mrad). µSTEM requires the user to specify the mean displacement, $\langle u^2 \rangle$, of the atoms in the simulation. These can be calculated from the Debye-Waller factors [50], B, often found in XRD experiments [51]

$$\left\langle u^2 \right\rangle = \frac{B}{8\pi^2}. \tag{3.4}$$

Debye-Waller factors from XRD measurements of Cu-SSZ-13 performed at 449 K were used in this work [14]. In QSTEM the user instead needs to specify a temperature for the frozen phonon displacement. In this work a temperature of 300 K was used and the results were averaged over 2 runs.

Finally, to get high-resolution images representative of experimental results we also need to add lens aberrations to the simulations. For these simulations we used typical aberration magnitudes for a FEI Titan 80-300 TEM with a C_s (spherical aberration) corrector (see Appendix C). The orientation of the aberrations was decided by randomizing an azimuthal angle for each aberration coefficient. The aberration parameters are summarized in Table 3.1 and were used for every simulation.

3.2.2 Multislice algorithm

Both simulation softwares, QSTEM ([41], [52], [53]) and µSTEM ([54]), are based on the multislice algorithm. In the first step of this algorithm, a large supercell is constructed from the provided model cell. The supercell is then divided into a number of slices of identical thickness, δt, and the atomic potential within each slice is projected to a two-dimensional potential [52], [55]. The incident electron beam is simulated by a modulated plane wave with the focused beam of a STEM probe represented by contributions from multiple plane waves [52], [54]. The projected potentials act as a kind of "phase grating" for the propagating electron beam in analogy with a beam of light propagating through a number of optical components

Aberration coefficient	Magnitude	Orientation of aberration (rad)
2-fold astigmatism	0.8 nm	2.62
3-fold astigmatism	41 nm	4.53
2nd order axial coma	14 nm	0.0
3rd order spherical	2.0 µm	-
4-fold astigmatism	2.0 µm	1.90
Star aberration	0.5 µm	0.92
5-fold astigmatism	89 µm	0.58
Three lobe aberration	16.5 µm	1.17
4th order axial coma	16.5 µm	2.17
5th order spherical	8.4 mm	-
6-fold astigmatism	234 µm	2.49

Table 3.1: Magnitude and orientation of aberration coefficients. The same set was used in all simulations. The magnitudes are based on Appendix C and the orientations were randomized.

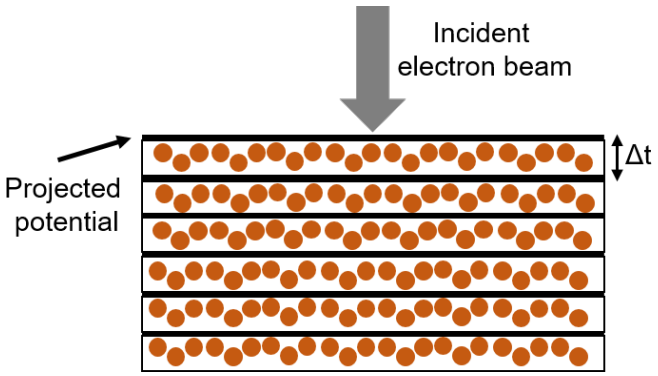

Figure 3.4: Concept of multislice method. The 3D atomic potential within each slice of thickness Δt is projected to a 2D plane. The wave function of the incident electron beam is multiplied with the 2D potential and then propagated through vacuum until the next 2D potential [52]. Figure adapted from [52].

in conventional optics [55]. This representation separates the scattering process into two parts: one part in which the electron beam interacts with projected 2D potential and a second part in which the resulting, scattered electron beam(s) propagate through vacuum [52] (see Fig. 3.4).

3.2.2.1 Inelastic scattering

An important feature that differs between implementations of the multislice algorithm is the way to handle inelastic thermal scattering. Two separate methods: the absorptive model and the frozen phonon model, are reviewed in this section. For the simulation software used here, QSTEM uses the frozen phonon representation while µSTEM can apply both models.

In the absorptive model, the electrons are "absorbed" by being completely removed from the simulation once they scatter thermally [54]. This means that mul-

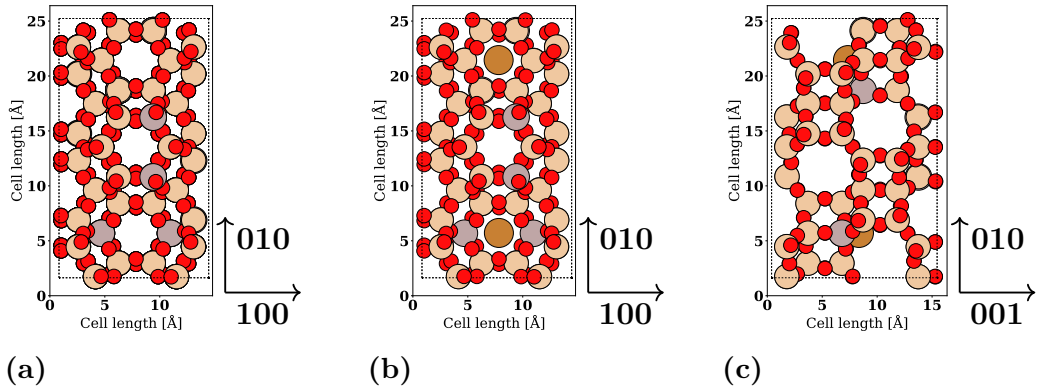

Figure 3.5: The orthorhombic simulation cell of SSZ-13. (a) Viewed along the [001]-direction and (b) with Cu added to the 6MR. (c) The same cell as in (b) but viewed along the [100]-direction. Light brown atoms are Si, brown atoms are Cu, red atoms are O and grey atoms are Al.

tiple thermal scattering events by the same electron is impossible in this representation. On the other hand, in the frozen phonon model, inelastic scattering is entirely omitted. Thermal scattering is instead represented by the electron beam scattering elastically against atoms that are slightly thermally displaced [52]. This method is based on the idea that the electrons in the electron beam travel much faster than the speed of the atom movement in thermal vibration [54]. The travelling electron therefore sees a "snap-shot" of the atoms, that appear to be frozen in mid-vibration, and the result is calculated from an average over multiple iterations [52], [54].

When comparing both models, the frozen phonon model has been shown to produce results more in line with experiments than the absorptive model, even though the former does not address inelastic scattering at all [54].

3.2.3 Model cell

An orthorhombic simulation cell consisting of Si and O atoms was constructed in the Atomic Simulation Environment software (ASE), see Fig. 3.5, [56] and modified to include Al and Cu atoms. A Si/Al ratio of 11:1 for the simulation cell was chosen since this most closely represented the experimental sample's 10:1 ratio without significantly altering the size of the cell.

Cu atoms were added to the simulation cell corresponding to the active sites in the 6MR (Fig. 3.5b) and the 8MR. Initially, only a single simulation unit cell (as in Fig. 3.5b and 3.5c) was repeated along the direction of view in the simulation software. This resulted in the Cu atoms being stacked in a column through the unit cells, which in turn yielded a very bright contrast for these atoms (see Fig. 4.6 in section 4.2). This ordered configuration is, however, highly unlikely in the real samples where Cu atoms would be more randomly positioned. Therefore, a new simulation cell was constructed consisting of five cells of the original simulation structure along the direction of the incident electron beam, having the Cu atoms dispersed among equal crystallographic sites (keeping the overall Cu ratio constant, see Fig. 3.6). This type of cell was, as in the case of the original cell, repeated in

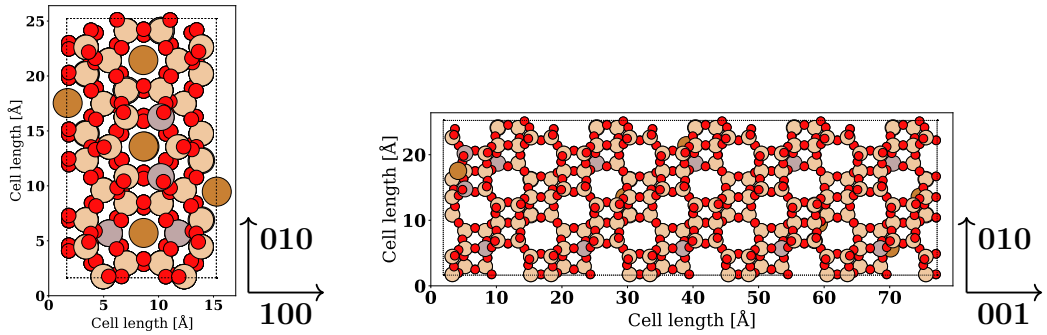

Figure 3.6: Expanded simulation cell of SSZ-13. (a) Viewed along the [001]-direction with Cu atoms dispersed among equal crystallographic sites to better represent a real sample. (b) The same cell as in (a) but viewed along the [100]-direction. Light brown atoms are Si, brown atoms are Cu, red atoms are O and grey atoms are Al.

the simulation forming a supercell with a thickness of about 200 nm.

3.3 Sample Preparation

Proper sample preparation is one of the most important factors in order to achieve high-resolution images in electron microscopy. To quote Russo (2016), "the major limiting factor for structure determination is specimen preparation" [57], and Williams and Carter (2009): "The quality of your data is at least directly proportional to the quality of your specimen (and this relationship is often far stronger than the linear nature just implied)" [30]. In this section, we will briefly describe our experimental samples together with a discussion on how they were prepared for electron microscopy. Two different methods, one well-proven from the literature and one developed in-house, were tried to disperse the sample on TEM grids in a manner well suited for high-resolution STEM imaging. These methods are described in section 3.3.2 and section 3.3.3 below.

3.3.1 SSZ-13 samples

The samples for this project were provided by Mike Schmithorst and Brad Chmelka of the Chmelka group of UCSB . Three different SSZ-13 samples with differing chemical compositions were supplied for this work: H-SSZ-13, Cu-SSZ-13 (3.3 wt%) Cu) and Pd-SSZ-13 (5 wt% Pd).

The H-SSZ-13 sample is free of infused metal ions. This means it can be used to acquire images of the zeolite framework without contribution from any metal ions. These images can then be used as reference images to compare against images of the samples with added metals of either Cu or Pd. This will be particularly important for the Cu sample since the signal of this element, according to the simulations in section 4.2, will already be relatively weak.

Pd have the ability to display the same ion-exchanged species, Pd^{2+} and $[Pd(OH)]^{+}$ [58], as Cu in section 2.2.2 and can supposedly thereby occupy the same active sites in the 6MR and 8MR of the zeolite framework. In this work, the advantage of the Pd sample is due to the Z^2 dependence of contrast in HAADF-STEM images where Pd consequently will be much more clearly distinguishable than Cu ions in the same positions. Having access to images of the Pd sample can thus potentially ease the image interpretation during the initial imaging of the Cu sample.

Figure 3.7: Cage setup for sample sonication in Branson 3800 ultra-sonic bath.

3.3.2 Sample preparation: Grinding method

Initially, a well-known and proven method of preparation for STEM imaging of zeolites was tried. In this method, the provided zeolite powder was ground for several minutes [39]–[41], [53], [59], [60] before a high-purity solvent of either ethanol or dichloromethane was added [39]–[41], [53], [59], [61]. A few drops were then applied to a holey carbon TEM grid [39]–[41], [45], [53], [59], [61], [62].

Unfortunately, this method of preparation turned out to be unfavourable for our samples. Even though the powder was ground for several minutes, a large amount of sizeable crystal clusters turned up on the grids (see Fig. 3.8a). This was problematic for atomic resolution STEM imaging where you preferably aim at many thin and isolated single-crystal particles. We therefore set out to try and optimize the preparation method.

3.3.3 Sample preparation: Ultrasonication method

The main idea of this method was to completely replace the grinding of the zeolite powder with sonication in order to more effectively disperse the nanocrystals. This approach has also been used before in the literature [42]. The powder and solvent

were prepared in a small glass bowl before the latter was inserted in a wire-suspended cage inside the ultrasonic bath (Fig. 3.7). After sonication, the solution was left to settle for a chosen amount of time. The expectation was that larger clusters would sink to the bottom of the bowl during this time. Finally, drops taken from the top of the solution were applied to the TEM grids.

Furthermore, 9 different parameters that could impact the preparation outcome were identified. We aimed to optimize these parameters for a high yield of STEM-suitable nanocrystals. These parameters are summarized in Table 3.2.

Parameters
Concentration of powder vs. solvent
Type of solvent
Type of grid (lacey or holey carbon)
Plasma cleaned grid?
Time for plasma cleaning grid
Type (power) of sonicator
Time for sonication
Time to let solution settle
Number of drops applied to the grid

Table 3.2: Variable parameters that were deemed to have a potential effect upon the TEM sample preparation process.

First it was decided that all grids would be plasma cleaned. This approach takes inspiration from cryo-electron microscopy where plasma cleaning is used to make grids more hydrophilic. This in turn helps spread applied drops more evenly over the grid's surface [57]. The time for plasma cleaning was limited to 10 s so as to not excessively damage the carbon support.

We soon decided to replace the holey carbon grids with lacey carbon since the latter offer a higher fraction of open void areas compared to the former (see Fig. 3.8a and 3.8b). This eased the process of finding SSZ-13 crystals not blocked by carbon support, a vital factor in order to attain atomic resolution images.

No qualitative difference was found between using dichloromethane or ethanol as solvent in the sample preparation. To rule out that the solvents on their own did not induce agglomeration of the nanocrystals, we also studied SSZ-13 powder fresh "out of the box" by scanning electron microscopy (SEM). The samples also showed agglomeration, see Fig. 3.8d for an example. The conclusion was therefore that no step in the preparation method itself was responsible for the agglomeration.

Two different kinds of ultrasonic baths were tried out, a Branson 3800 and a Branson 200. The 200-model was quickly excluded since it was not powerful enough.

Altogether, this left us with four parameters left to study:

- Concentration of powder vs. solvent
- Time for sonication
- Time to let solution settle
- Number of drops applied to the grid

A qualitative study of how these parameters affect the outcome of the specimen preparation is presented in section 4.1.

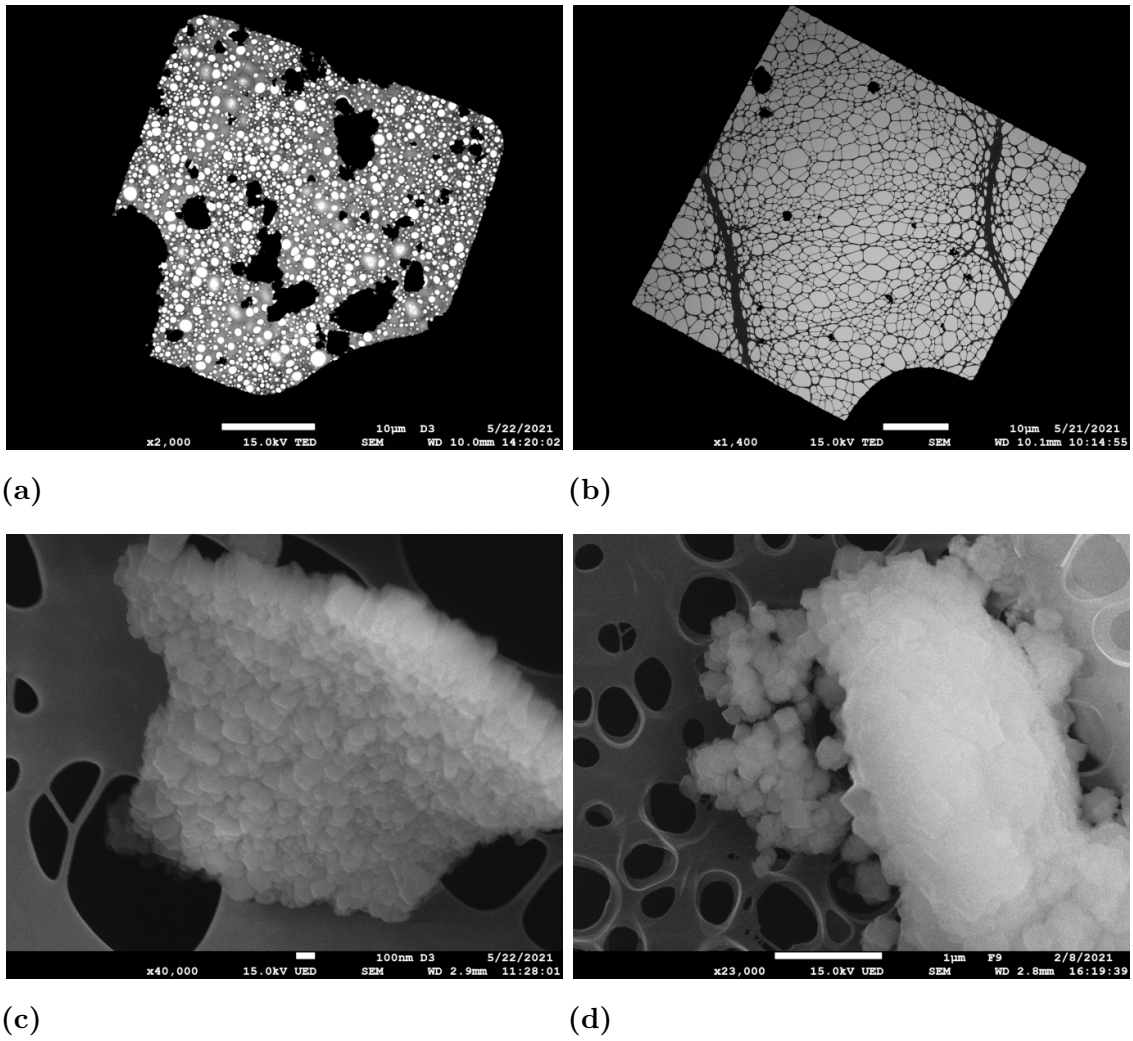

(a) **(b)**

(c) **(d)**

Figure 3.8: STEM BF images of representative squares from a grid prepared with (a) the grinding and (b) the ultrasonication method (b). SSZ-13 is shown as dark clusters on the supporting, net-like carbon structure. Note the difference in open area between a holey carbon grid (a) and a lacey carbon grid (b). Examples of SSZ-13 agglomerates from (c) ultra-sonication method and (d) fresh, unprocessed sample. Scale bar: 10 µm (a,b), 1.0 µm (d), 100 nm (c). All images were taken at an acceleration voltage of 15 kV.

3.3.4 Methods to avoid moisture exposure

As stated in section 3.1.4.1, exposure to moisture is believed to negatively impact the lifetime of the zeolite in the electron beam of the microscope. This has been handled to varying degrees in earlier works who have performed high-resolution imaging of other zeolites. Some studies have stored the samples inside the argon atmosphere of a glove box [41], [45], [46], kept the zeolite for an extended time in high-vacuum [60] or heated the sample to burn away absorbed water before imaging [62]. Other studies have not mentioned any precautions made to avoid exposure to moisture indicating that this was not a limiting factor in their studies [53], [59], [61].

Keeping in mind the possible effect of moisture, we set out to explore the above stated types of storage. The undoped H-SSZ-13 sample was stored in ambient conditions and could, when called for, be heated in the microscope stage with a Philips PW 6592/05 Heating Holder. After discussions with UCSB, we decided to follow a heating protocol where the temperature was increased by 5 °C per minute to 450 °C. This temperature was then held for one hour. The Pd-SSZ-13 and Cu-SSZ-13 samples were stored inside an argon-filled glove box. These samples were transferred to the microscope in a parafilm sealed encasing, experiencing a total air exposure less than 30 s.

4

Results and discussion

This chapter summarises the main results of this thesis. The first section describes a qualitative study of the ultra-sonication method first described in section 3.3.3. Here we particularly evaluate the yield and size distribution of particles. In section 4.2 we show results from our simulations of STEM images of Cu-SSZ-13. In the last section, we present results of HAADF-STEM imaging of our SSZ-13 samples.

4.1 Qualitative study of the ultra-sonication method

We conducted a qualitative study where we investigated the impact of varying the above four parameters: concentration, time for sonication, time to let solution settle and number of drops applied to the TEM grid. The aim of the study was to find which specifications yielded (1) a high number (yield) of particles around the middle of the grid and (2) clusters with a suitable size for atomic resolution STEM imaging. The study was conducted over 15 different batches, with the 10 most promising presented here. Between each batch, one or several parameters were tweaked. The parameters for each batch are provided in Appendix A.

To evaluate aspect (1), we counted the number of particles found in the four squares closest to the middle of the grid (see Fig. 4.1). The results over our ten batches are presented in Fig. 4.1b. In order to assess aspect (2), we divided all particles discovered in the four central squares into four approximate size categories: $\geq$ 1 µm, 700-900 nm, 300-600 nm and 100-200 nm. Examples of particle clusters with said dimensions are shown in Fig. 4.2 and the resulting size distributions are presented in Fig. 4.3.

Isolated, single-crystal particles overhanging a void in the carbon support are preferable for the high-resolution imaging. One of the most evident types of single-crystal particles are the cubic shaped particles found, for example, in Figs. 3.8d and 4.2b. These particles have a typical size of around 200 nm and are consequently seldom found in the smallest (100-200 nm) category of clusters. The largest clusters on the other hand ($\geq$ 1 µm), are in general far too thick for atomic imaging. Thus, we focused on trying to increase the yield of clusters in the 700-900 nm and 300-600 nm categories. Batch G produced a promising fraction of particles in these categories (Fig. 4.3) while also yielding a promising number of particles in the centre of the grid (Fig. 4.1b). Therefore, the specifications used in the creation of this batch was chosen as the base for the continued study (see Appendix A for specific values of the parameters).

Next, we wanted to further study how the number of drops applied to grids affected the results. Three samples were prepared from a new batch, G', using the same specifications as for batch G but varying the number of drops applied to each TEM grid. The resulting particle yield and size distribution are presented in Figs. 4.4 and 4.5 respectively.

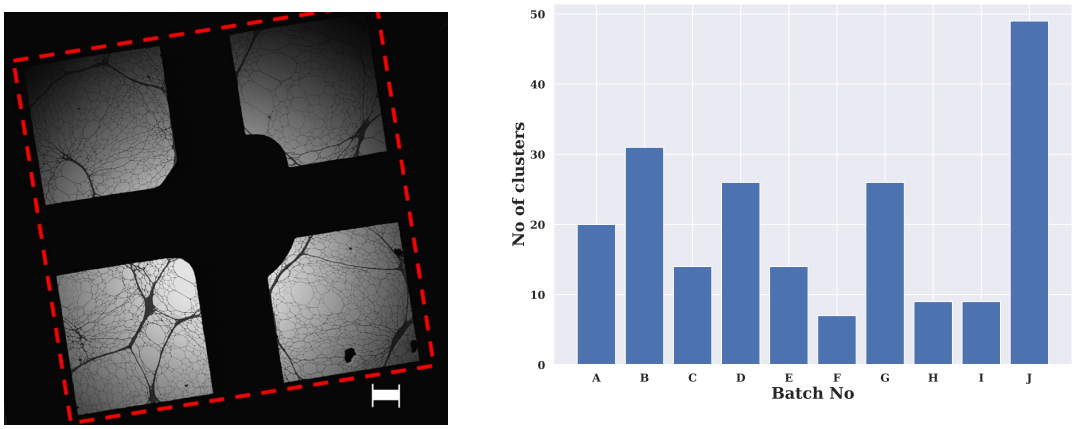

(a) **(b)**

Figure 4.1: (a) STEM bright-field image of one of the samples used in the qualitative evaluation of the ultra-sonication method. The central four squares of the TEM grid are outlined with a red, dotted square. Scale bar is 10 µm. (b) A histogram showing the number of particle clusters found in the four central squares of the grid for ten batches A-J. The parameters for each batch are provided in Appendix A.

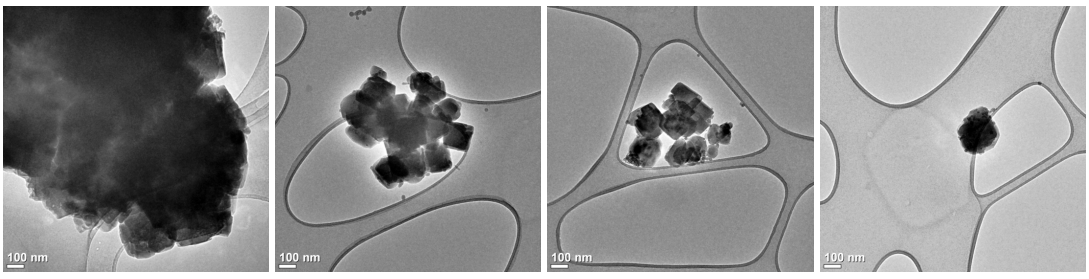

(a) **(b)** **(c)** **(d)**

Figure 4.2: Bright-field TEM images showing examples of particle clusters corresponding to the four different size categories used in the size distribution evaluation: (a) $\geq$ 1 µm, (b) 700-900 nm, (c) 300-600 nm and (d) 100-200 nm. All images were taken at an acceleration voltage of 200 kV.

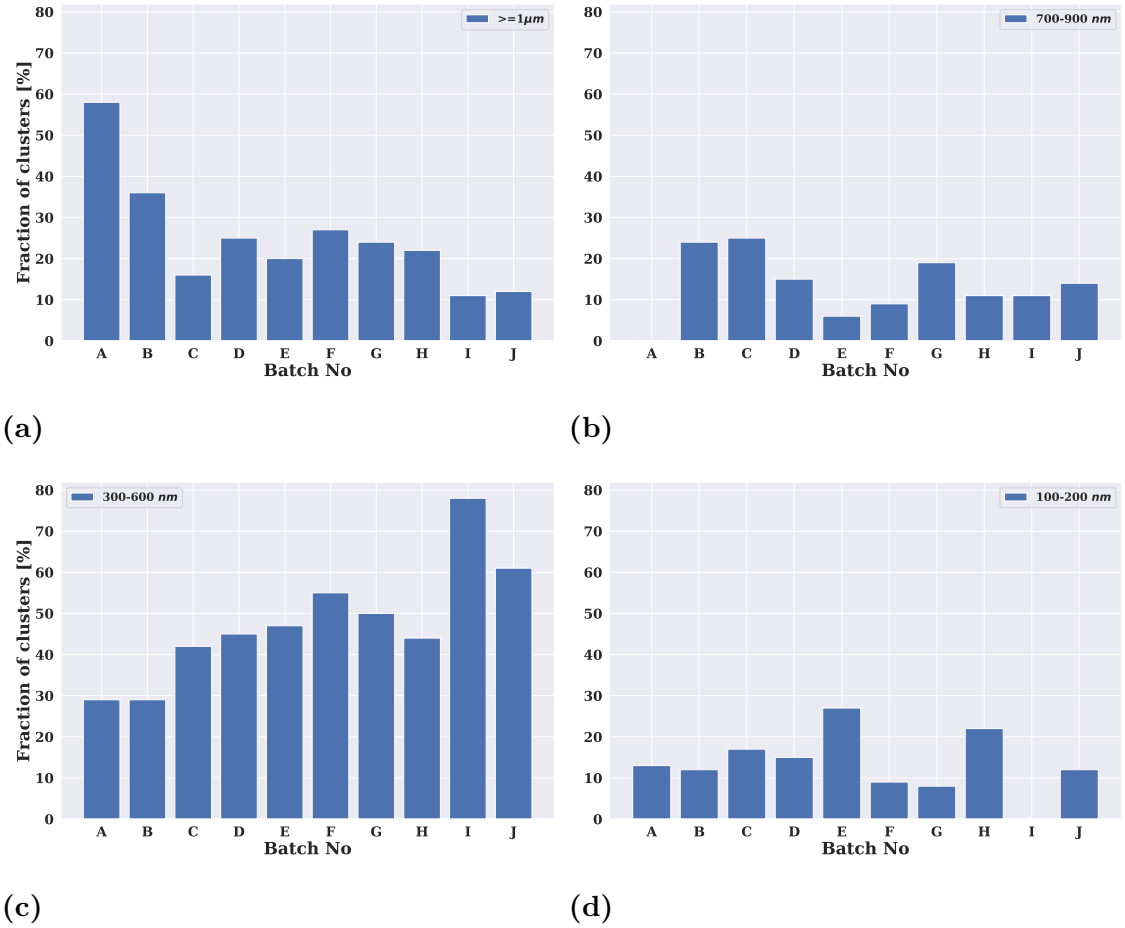

Figure 4.3: Histograms showing the size distribution of particles in the central four squares of the TEM grid for ten batches A-J. The parameters for each batch are provided in Appendix A. The bars represent the fraction (in %) of particles categorized as having a dimension of (a) $\geq$ 1 µm, (b) 700-900 nm, (c) 300-600 nm and (d) 100-200 nm.

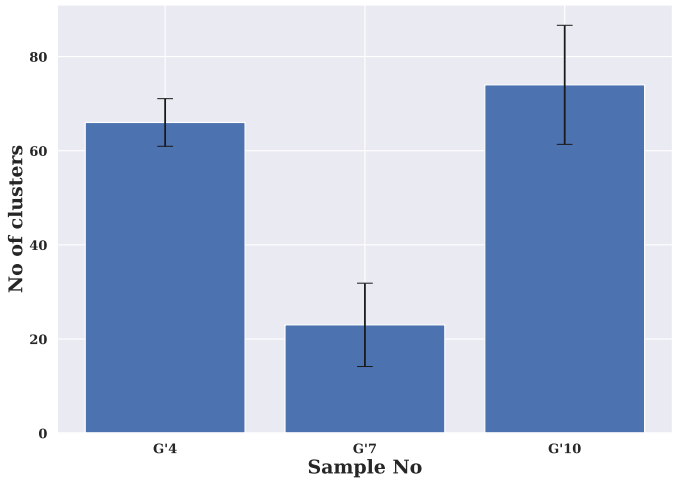

Figure 4.4: Histograms showing the number of particle clusters found in the central four squares of each grid for sample G'4, G'7 and G'10. The samples have been prepared using the parameters of batch G in Appendix A and the number in each sample name represents the number of drops applied to the grid. For a discussion about the error estimation, see Appendix B.

The deviating results of sample G'7 in Fig. 4.4 should be noted. The counting statistics in this analysis hinders us from drawing any solid conclusions. However, the indications is, that the result is highly variable as a function of applied number of drops and that the error estimation applied in Fig. 4.4 is not taking all aspects into account (see Appendix B for a further discussion). Furthermore, the difference in particle yield (Fig. 4.4) and size distribution (Fig. 4.5) is not significant when applying either 4 or 10 drops to the grid.

An explanation for the discrepancies discussed in Fig. 4.4 and 4.5 could be that the pipettes used in the sample preparation (standard 10 ml glass pipettes) form too large drops. Massive drops that essentially "flush away" most of the sample that was applied with the last drop could potentially explain the high variance (sample G'7) together with the lack of significant change in result with increased number of applied drops (sample G'4 and G'10). This effect could be investigated by applying smaller drops, for example by using a micropipette or by dripping the solution from the tip of a pair of tweezers.

4.2 Simulation results

The simulated high-resolution images using the absorptive model viewed along the [001] with Cu dispersed among the 6MR are shown in Fig. 4.7. The contrast of the Cu atoms in Fig. 4.6 is significantly weaker than in Fig. 4.7. This difference emphasises the strong dependence of the Cu signal on the stacking of many Cu atoms along the line of view. We can easily imagine a case where the Cu atoms turns out to be nearly invisible at a low Cu concentration, especially if one would also add

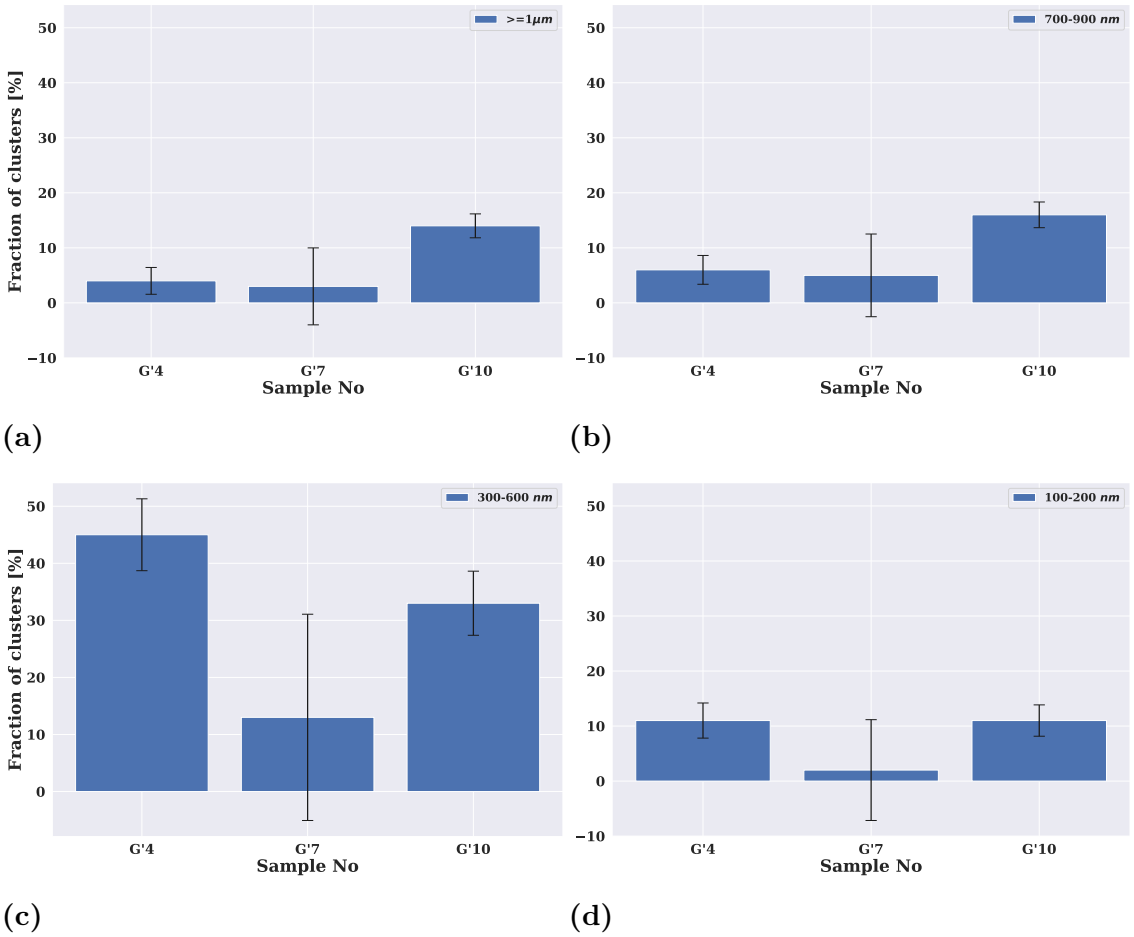

Figure 4.5: Histograms showing the size distribution of particles in the central four squares of each grid for sample G'4, G'7 and G'10. The samples have been prepared using the parameters of batch G (Appendix A) but varying the number of drops applied to each TEM grid, which is represented by the number in each sample name. For a discussion about the error estimation, see Appendix B.

the background noise inherent to experimental images. This clearly illustrates the advantage of using Pd samples, due to their innately stronger signal, during the initial imaging process (as described in section 3.3.1).

The active sites can in principle be determined by examining high-resolution images recorded along the [001] and [100] directions respectively. When the cations are located in the 6MR, there is a slight increase in signal from said rings imaged along the [001] direction (Fig. 4.8a) compared to when the Cu atoms are located in the 8MR (Fig. 4.8c). The reversed argument holds for the 8MR and the [100] direction (Fig. 4.8b and 4.8d). In both cases however, the simulations show that the signal of the Cu atoms can be expected to be very weak and difficult to distinguish by eye.

The difference between using the absorptive model for inelastic scattering and the frozen phonon model is illustrated in Fig. 4.9. The QSTEM high-resolution image (Fig. 4.9b) is noisier than the µSTEM high-resolution image (Fig. 4.9a), most probably due to the averaging of thermal displacements in the QSTEM frozen phonon model. Nevertheless, comparing the contrast of the Cu atoms of the two methods, the added noise does not significantly affect the visibility of the Cu atoms (Fig. 4.9c and 4.9d).

Additional simulated high-resolution images can be found in Appendix D.

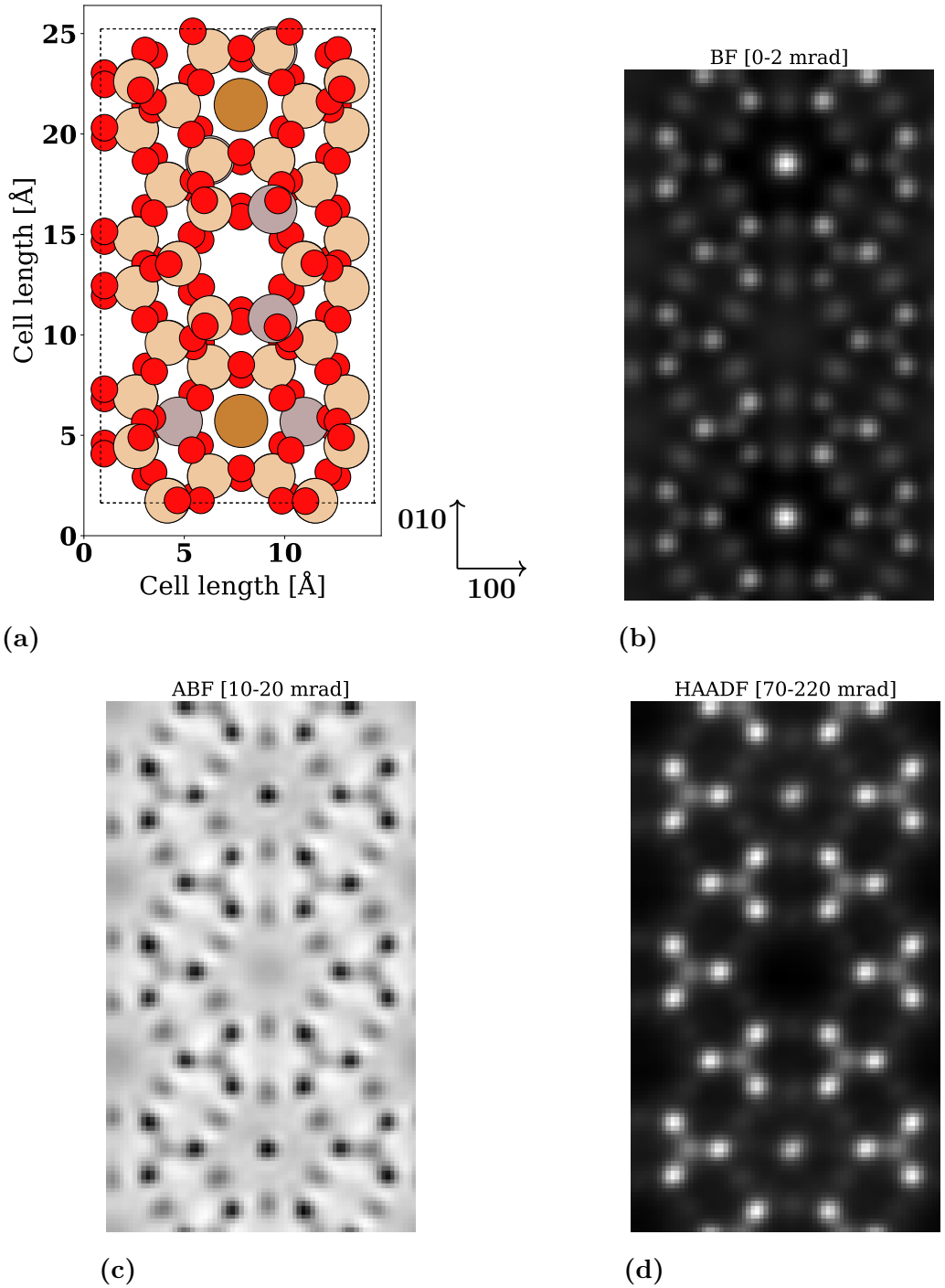

Figure 4.6: Simulated high-resolution images along the [001]-direction in µSTEM using the absorptive model with Cu in complete atomic columns within the 6MR. (a) The model cell. Light brown atoms are Si, brown atoms are Cu, red atoms are O and grey atoms are Al. (b) Simulated BF image, (c) ABF image and (d) HAADF image. Note the high contrast of the Cu atoms in (b-d). This effect is due to the stacking of Cu atoms as complete atomic columns. Note the contrast reversal in (b).

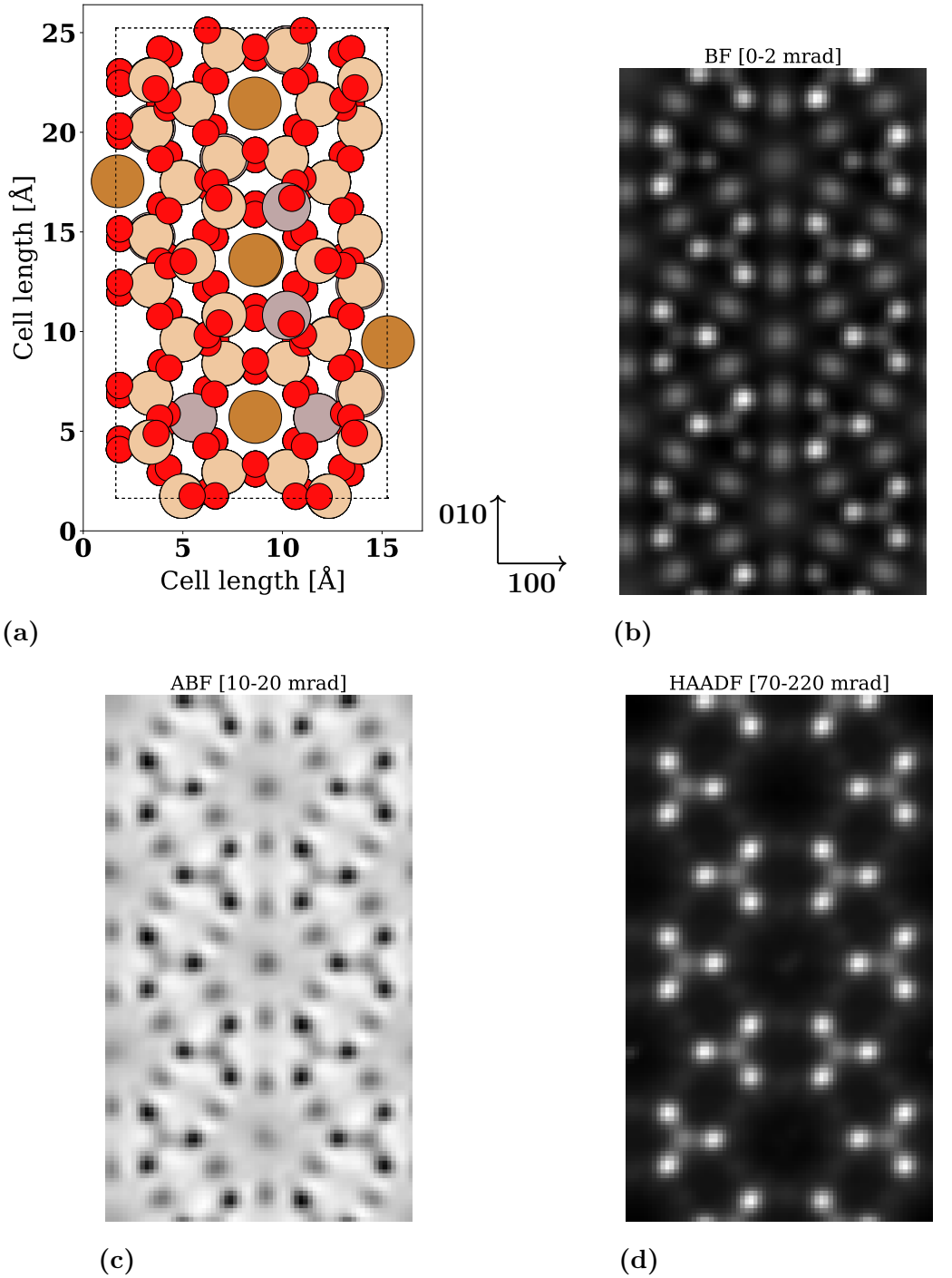

Figure 4.7: Simulated high-resolution images along the [001]-direction in µSTEM using the absorptive model with Cu dispersed among equal crystallographic 6MR sites. (a) The model cell. Light brown atoms are Si, brown atoms are Cu, red atoms are O and grey atoms are Al. (b) Simulated BF image, (c) ABF image and (d) HAADF image. Note the contrast reversal in (b).

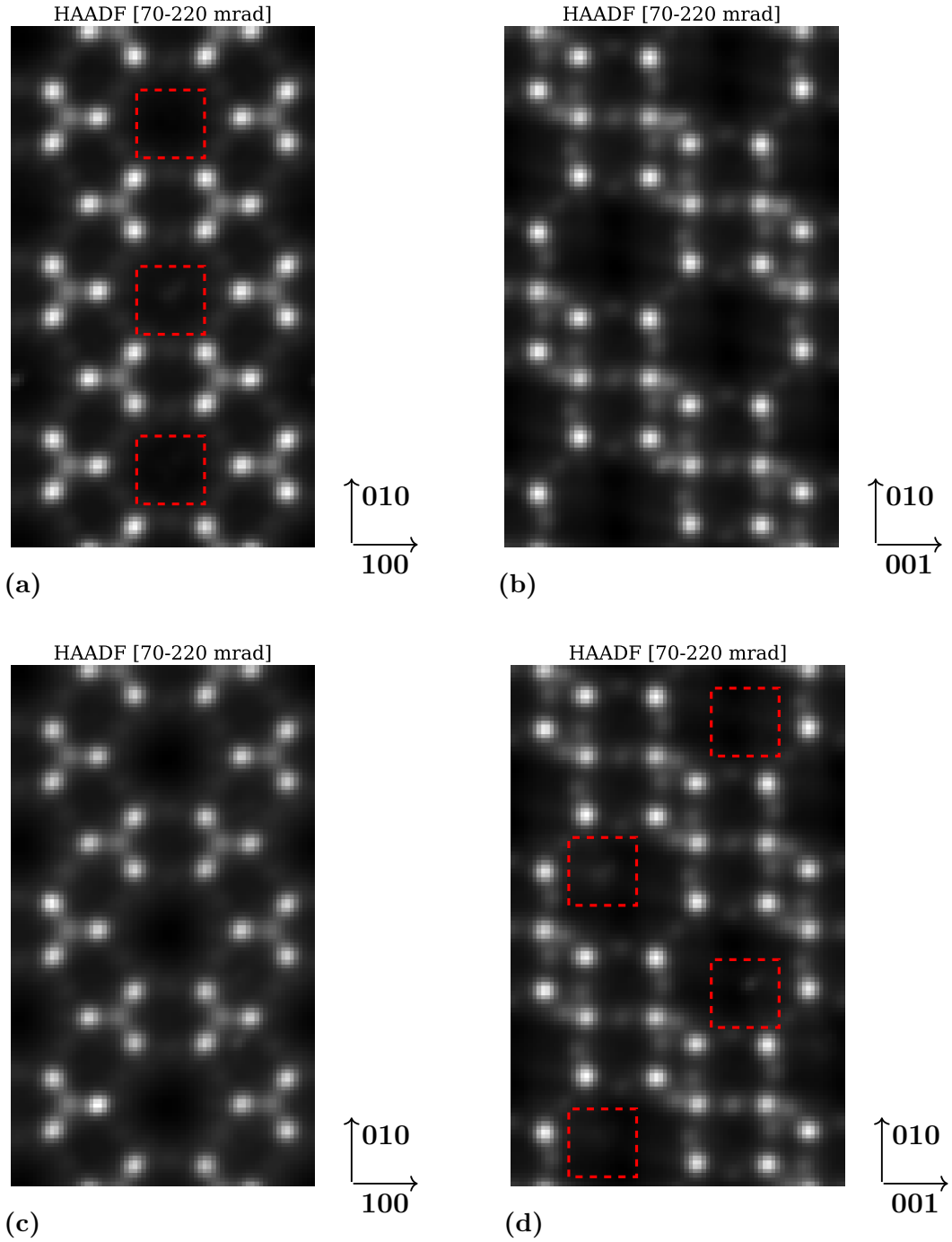

Figure 4.8: Simulated HAADF high-resolution images in µSTEM using the absorptive model with (a-b) Cu dispersed among equal crystallographic 6MR sites and (c-d) 8MR sites. (a, c) Structure viewed along the [001]-direction and (b, d) along the [100]-direction. Sites where Cu is located have been highlighted with a red square.

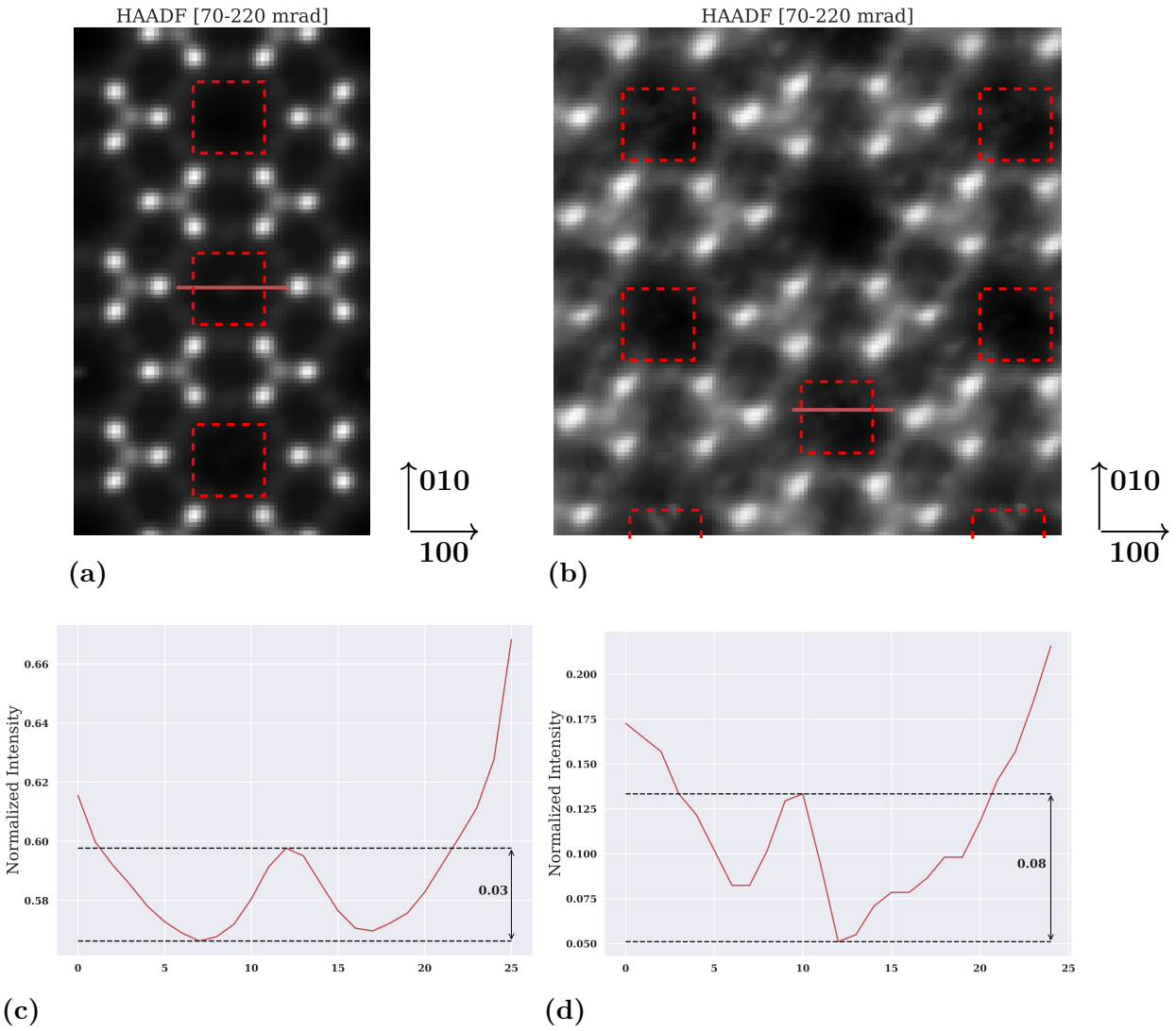

Figure 4.9: Comparison between HAADF high-resolution images simulated in (a) μSTEM using the absorptive model and (b) QSTEM using the frozen phonon model. The structure is viewed along the [001]-direction and Cu is dispersed among equal crystallographic 6MR sites. Sites where Cu is located have been highlighted with a dashed red square. (c, d) Line profiles (solid red lines) over a Cu atomic column in (a, b) respectively. The magnitude of the Cu peak from the baseline (in units of normalized intensity) is shown between the two dotted black lines.

4.3 Microscopy studies

HAADF-STEM imaging was performed on H-SSZ-13 and Pd-SSZ-13 using low-dose conditions. This meant using a low magnification, a large defocus and Kikuchi lines to limit radiation damage while tiling suitable nanocrystals to the closest zone axis. Unfortunately, electron beam damage was too severe in all cases to achieve atomic resolution.

Independent of storage conditions for the H-SSZ-13 samples, we managed to image atomic planes (Figs. 4.10 and 4.11) on a FEI Titan 80-300 microscope operated at an acceleration voltage of 300 kV. The damage rate was, however, very high (on the order of a few seconds for severe damage). This meant the focusing of the electron probe could not be performed multiple times on the same area intended for imaging. After having focused or acquired one image we had to quickly move to another area and hope that the same focus conditions would still apply.

We saw no significant difference in damage rate between the dehydrated and the non-dehydrated samples. Our results here cannot rule out the effect of hydration on damage rate, but they do imply that other, unknown damage effects are more dominant.

Fig 4.10 shows high resolution STEM images where a set of planes has been imaged. Two frequency space filters have been applied to the data in order to more clearly distinguish the atomic planes in Figs. 4.10d and 4.11d [63]. The purpose of the first, a Wiener filter, is to remove contributions from amorphous phases by separating the discrete spots of a crystalline material from the background [64]. The second is a Butterworth filter which removes high frequency components, the effect of which can be clearly observed in the FFTs of Figs. 4.10d and 4.11d [64]. The lattice fringe spacing in Figs. 4.10 and 4.11 correspond to an interplanar distance of $d \approx 9$ Å. This distance is in approximate agreement with the 100 crystal planes of chabazite (the naturally occurring variant of SSZ-13) with a d of 9.4 Å [65].

After we had attained images of H-SSZ-13 showing atomic planes, we expected Pd-SSZ-13 and Cu-SSZ-13 to be more stable and less prone to electron beam damage. This expectation was partly due to the fact that these samples never had been exposed to ambient conditions and partly from an anticipation that the included metal atoms could stabilize the zeolite framework. We began by investigating the Pd-SSZ-13 sample since the Z-contrast of HAADF imaging would make the Pd atoms more evident than their Cu counterparts in Cu-SSZ-13. Unexpectedly, it was more difficult to image the atomic planes. The Pd-SSZ-13 was investigated at 200 kV using low-dose conditions in a JEOL Mono NEO ARM 200F microscope (called the ARM microscope henceforth). This led us to suspect that the acceleration voltage could be a dominant factor for the damage, with less damage at 300 kV than at 200 kV.

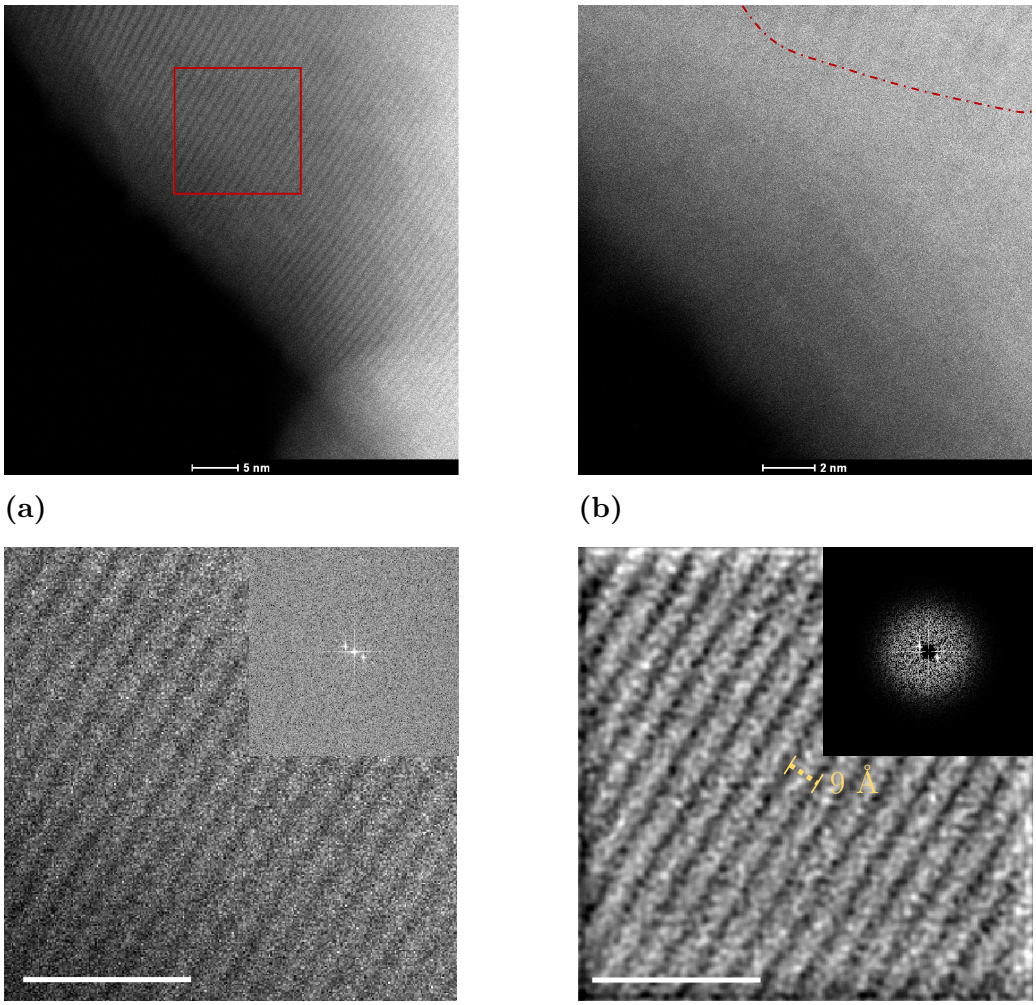

(a) **(b)**

(c) **(d)**

Figure 4.10: (a) HAADF-STEM image of H-SSZ-13 showing atomic planes. The image was taken at an acceleration voltage of 300 kV. The sample was stored in ambient conditions and dehydrated in the microscopy stage before imaging. (b) The same area as in (a) a few (≈3) seconds later. The contrast from the atomic planes have mostly disappeared due to amorphization from quick electron beam damage. A few weak lines can be observed in the top right of the figure (outlined by a red, dashed line for clarity). (c) The area outlined by a solid red square in (a) and the corresponding FFT pattern (inset). (d) Same image as in (c) with Butterworth and Wiener filters applied. The line spacing corresponds to an interplanar distance of about 9 Å. Scale bar: 5.0 nm (a, c, d), 2.0 nm (b).

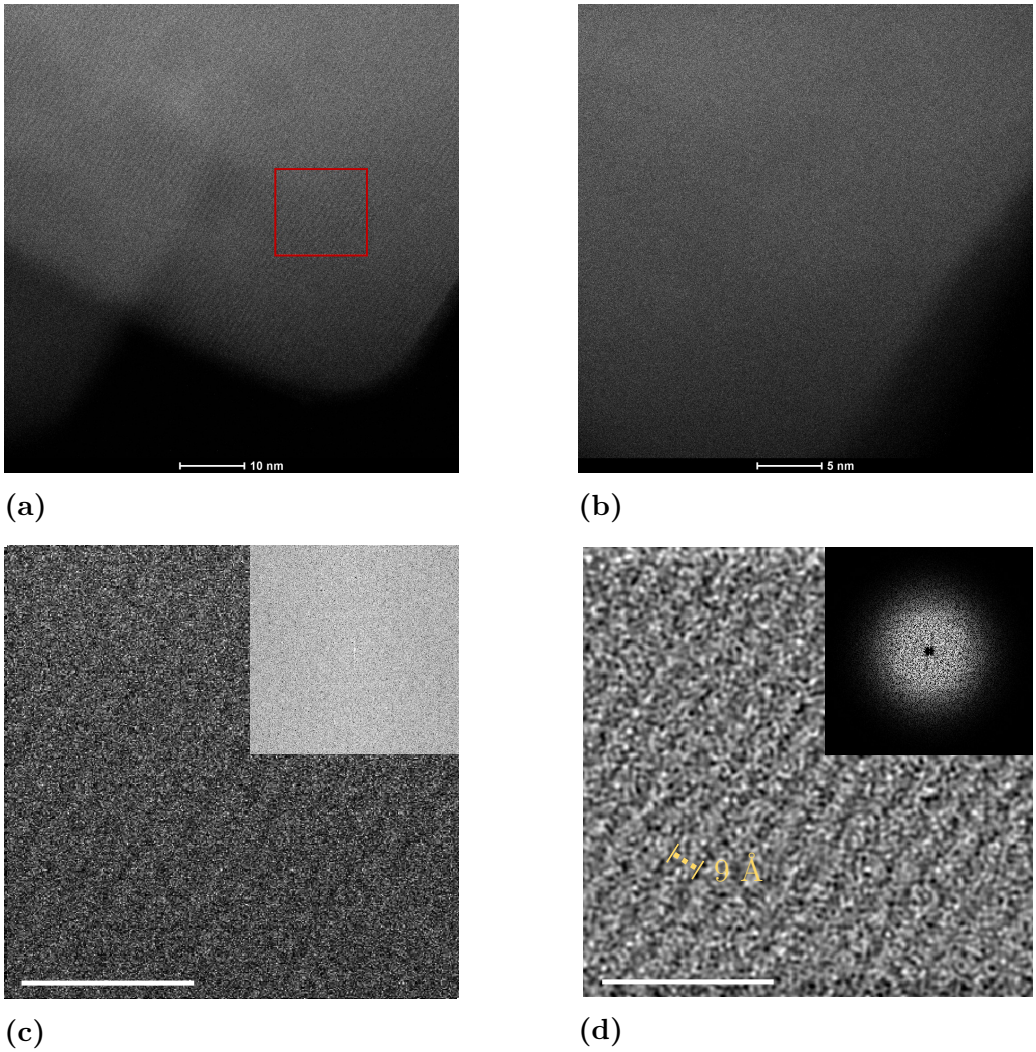

(a) **(b)**

(c) **(d)**

Figure 4.11: (a) HAADF-STEM image of H-SSZ-13 showing atomic planes. The image was taken at an acceleration voltage of 300 kV. The sample was stored in ambient conditions and not dehydrated before imaging. (b) The same area as in (a) a few ($\approx$ 3) seconds later. The contrast from the atomic planes have disappeared due to amorphization from quick electron beam damage. (c) The area outlined by a solid red square in (a) and the corresponding FFT pattern (inset). (d) Same image as in (c) with Butterworth and Wiener filters applied. The line spacing corresponds to an interplanar distance of about 9 Å. Scale bar: 10.0 nm (a), 5.0 nm (b, c, d).

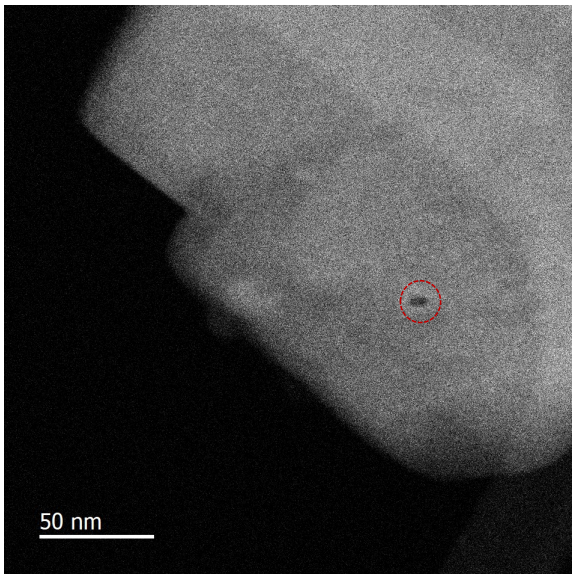

Figure 4.12: Low-magnification HAADF-STEM image of Pd-SSZ-13. The image was taken at an acceleration voltage of 200 kV. The sample was stored in a glove box and was transferred to the microscope in a parafilm sealed encasing, experiencing a total air exposure less than 30 s. Note the beam induced damage (outlined with the dashed, red circle).

Based on these observations of the visibility of atomic planes, we qualitatively investigated Kikuchi line fading in the diffraction patterns since they represent atomic planes in real space. Using low-dose conditions in the ARM microscope, we found that all lines faded with time and had completely disappeared after ≈ 1.5 s close to the edge of a particle and ≈ 6 s closer to the centre. In a FEI Tecnai T20 microscope operated at the same acceleration voltage, however, the Kikuchi lines of the undoped H-SSZ-13 sample survived for significantly longer. In a few cases almost up to one minute. It is known that the electron dose is an important parameter. The difference in damage rate between the ARM and the Tecnai microscope indicates that the electron dose plays a significant role. We do, however, need to further investigate the beam currents under the imaging conditions used in the two microscopes to be able to draw any solid conclusions.

Also, observations of thickness dependent Kikuchi line fading indicate that the damage is thickness dependent.

Even though it's not straightforward to directly compare different studies it should be noted that the electron beam sensitivity increases as the Si/Al ratio decreases. Our samples have a Si/Al ratio of 10, but investigations on other zeolites with a Si/Al ratio as low as 1 have achieved atomic resolution images using similar methods [39], [41], [59], [66]. This could indicate that there are further parameters to discover about the damage mechanisms for this type of material, beside the predominantly stated factors of hydration level and Si/Al ratio.

With all this in mind, we saw no indications that the Cu-SSZ-13 samples would be any more stable than the H-SSZ-13 and PD-SSZ-13. At least using the methods employed here. We therefore decided not to try and image the Cu sample until we

know more about the damage mechanisms of these materials.

To summarize, we have observed thickness dependent damage of H-SSZ-13 and Pd-SSZ-13 samples. The rate of damage is likely related to the electron dose received by the specimen as well as potential, yet unknown, material-specific damage mechanisms. The effect of hydration on damage rate has been found to be negligible in comparison to these other effects.

5

Conclusions and outlook

This work concerns catalysts and the optimisation of atomic structure to increase the catalytic efficiency and lifetime of said systems. Catalysts are used in many different applications, for example vehicles, chemical synthesis, biological reactions and food processing. Today, most commercial heavy-duty vehicles rely on urea-based Selective Catalytic Regulations (SCR) to convert harmful nitrogen oxides (NO_x) into nitrogen NO_2 and water. The increasingly stringent regulations regarding vehicular emissions have brought about an intense research in automotive catalyst systems during the last decades. Among the leading candidates for state-of-the-art SCR systems are zeolites infused with transition metal ions. The metal cations, such as Cu and Pd, serve as active sites for the catalyst reaction. As with any catalyst, the position of the active sites in relation to the rest of the molecular structure is imperative for a full understanding of the system. For the zeolite system Cu-SSZ-13 studied in this work, two locations for its active Cu sites have been put forward during the last years. However, site-specific studies of the two active sites, such as high-resolution electron microscopy, are in general missing. This can to some degree be attributed to zeolites having a strong susceptibility to become heavily damaged by electron beam irradiation.

The aim of this work was to study methods for imaging and specimen preparation that limit electron beam damage to a degree that enables atomic resolution imaging of Cu-SSZ-13. The importance of proper specimen preparation can't be stressed enough. To be able to image with atomic resolution, it is important to have thin specimens to avoid multiple scattering and without overlap between SSZ-13 crystals. In order to better disperse and increase the yield of zeolite particles suitable for high-resolution microscopy on our TEM grids, we have opted forgo the standard grinding method in favor of using ultra-sonication. After evaluation of the latter method, we note that the concentration of zeolite powder and the time for the solution to settle after sonication are of particular importance. The performance of the ultra-sonication method should be further investigated with increased counting statistics, especially with a focus on how the particle yield and size distribution depend on the number of drops applied to the TEM grid.

We have also conducted simulations of HAADF-STEM images to assess the visibility criteria for Pd and Cu atoms within the zeolite framework. The simulations have been performed using two multislice algorithms simulating the thermal diffuse scattering of electrons. This renders an atomic number contrast that can be used to deduce the positions of the Pd and Cu atoms. These will be used to support experimental results of future works.

Finally, in the preparations for high-resolution imaging, we have observed the effects of electron beam damage on the sample. We have qualitatively seen an effect of electron dose and sample thickness on the damage rate. However, despite the fact that previous works have reported effects of hydration degree of the zeolite, we have not seen this as a limiting factor for the damage rate.

We conclude that there is still much to learn about the damage mechanisms in SSZ-13. They need to be further unravelled in order to develop optimal imaging procedures to limit electron beam damage. The continued studies on SSZ-13 should quantitatively investigate the damage process in more detail, with a specific focus on the effect of electron dose on the damage rate. This can be performed by, for example, studying diffraction spot fading while closely monitoring the beam current. Beyond the effect of Si/Al ratio, it would also be of interest to investigate how the rate of damage changes with different zeolite framework types (spatial structure) and dopant materials (such as Cu and Pd).

Bibliography

[1] B. Guan, R. Zhan, H. Lin, and Z. Huang, "Review of state of the art technologies of selective catalytic reduction of NOx from diesel engine exhaust", *Applied Thermal Engineering*, vol. 66, no. 1-2, pp. 395–414, 2014, ISSN: 13594311. DOI: 10.1016/j.applthermaleng.2014.02.021.

[2] J. H. Kwak, R. G. Tonkyn, D. H. Kim, J. Szanyi, and C. H. Peden, "Excellent activity and selectivity of Cu-SSZ-13 in the selective catalytic reduction of NOx with NH3", *Journal of Catalysis*, vol. 275, no. 2, pp. 187–190, 2010, ISSN: 00219517. DOI: 10.1016/j.jcat.2010.07.031.

[3] M. Castagnola, J. Caserta, S. Chatterjee, H. Y. Chen, R. Conway, J. Fedeyko, W. Klink, P. Markatou, S. Shah, and A. Walker, "Engine performance of Cu- and Fe-based SCR emission control systems for heavy duty diesel applications", *SAE 2011 World Congress and Exhibition*, no. 2, 2011, ISSN: 2688-3627. DOI: 10.4271/2011-01-1329.

[4] T. V. Johnson, "Review of Selective Catalytic Reduction (SCR) and Related Technologies for Mobile Applications", in *Urea-SCR Technology for deNOx After Treatment of Diesel Exhausts*, I. Nova and E. Tronconi, Eds., Springer, 2014, ch. 1, pp. 3–31, ISBN: 9781489980700. DOI: 10.1007/978-1-4899-8071-7_1.

[5] L. Xu, R. McCabe, W. Ruona, and G. Cavataio, "Impact of a Cu-zeolite SCR catalyst on the performance of a diesel LNT+SCR system", *SAE Technical Papers*, 2009, ISSN: 26883627. DOI: 10.4271/2009-01-0285.

[6] Y. Gu and W. S. Epling, "Passive NOx adsorber: An overview of catalyst performance and reaction chemistry", *Applied Catalysis A: General*, vol. 570, no. November 2018, pp. 1–14, 2019, ISSN: 0926860X. DOI: 10.1016/j.apcata.2018.10.036. [Online]. Available: https://doi.org/10.1016/j.apcata.2018.10.036.

[7] G. Cavataio, J. Girard, J. E. Patterson, C. Montreuil, Y. Cheng, and C. K. Lambert, "Laboratory testing of urea-SCR formulations to meet tier 2 bin 5 emissions", *SAE Technical Papers*, vol. 2007, no. 724, pp. 776–790, 2007, ISSN: 26883627. DOI: 10.4271/2007-01-1575.

[8] J. Song, Y. Wang, E. D. Walter, N. M. Washton, D. Mei, L. Kovarik, M. H. Engelhard, S. Prodinger, Y. Wang, C. H. Peden, and F. Gao, "Toward Rational Design of Cu/SSZ-13 Selective Catalytic Reduction Catalysts: Implications from Atomic-Level Understanding of Hydrothermal Stability", *ACS Catalysis*, vol. 7, no. 12, pp. 8214–8227, 2017, ISSN: 21555435. DOI: 10.1021/acscatal.7b03020.

[9] Y. J. Kim, J. K. Lee, K. M. Min, S. B. Hong, I. S. Nam, and B. K. Cho, "Hydrothermal stability of CuSSZ13 for reducing NOx by NH3", *Journal of Catalysis*, vol. 311, pp. 447–457, 2014, ISSN: 00219517. DOI: 10.1016/j.jcat.2013.12.012.

[10] K. Kharas, H. Robota, and D. Liu, "Deactivation in Cu-ZSM-5 lean-burn catalysts", *Applied Catalysis B: Environmental*, vol. 2, no. 2-3, pp. 225–237, Jun. 1993, ISSN: 09263373. DOI: 10.1016/0926-3373(93)80050-N. [Online]. Available: https://linkinghub.elsevier.com/retrieve/pii/092633739380050N.

[11] J. H. Kwak, H. Zhu, J. H. Lee, C. H. Peden, and J. Szanyi, "Two different cationic positions in Cu-SSZ-13?", *Chemical Communications*, vol. 48, no. 39, pp. 4758–4760, 2012, ISSN: 1364548X. DOI: 10.1039/c2cc31184d.

[12] F. Giordanino, P. N. Vennestrøm, L. F. Lundegaard, F. N. Stappen, S. Mossin, P. Beato, S. Bordiga, and C. Lamberti, "Characterization of Cu-exchanged SSZ-13: A comparative FTIR, UV-Vis, and EPR study with Cu-ZSM-5 and Cu-β with similar Si/Al and Cu/Al ratios", *Dalton Transactions*, vol. 42, no. 35, pp. 12 741–12 761, 2013, ISSN: 14779226. DOI: 10.1039/c3dt50732g.

[13] A. Godiksen, F. N. Stappen, P. N. Vennestrøm, F. Giordanino, S. B. Rasmussen, L. F. Lundegaard, and S. Mossin, "Coordination environment of copper sites in Cu-CHA zeolite investigated by electron paramagnetic resonance", *Journal of Physical Chemistry C*, vol. 118, no. 40, pp. 23 126–23 138, 2014, ISSN: 19327455. DOI: 10.1021/jp5065616.

[14] D. W. Fickel and R. F. Lobo, "Copper coordination in Cu-SSZ-13 and Cu-SSZ-16 investigated by variable-temperature XRD", *Journal of Physical Chemistry C*, vol. 114, no. 3, pp. 1633–1640, 2010, ISSN: 19327447. DOI: 10.1021/jp9105025.

[15] S. T. Korhonen, D. W. Fickel, R. F. Lobo, B. M. Weckhuysen, and A. M. Beale, "Isolated Cu2+ ions: Active sites for selective catalytic reduction of NO", *Chemical Communications*, vol. 47, no. 2, pp. 800–802, 2011, ISSN: 1364548X. DOI: 10.1039/c0cc04218h.

[16] A. Kato, S. Matsuda, T. Kamo, F. Nakajima, H. Kuroda, and T. Narita, "Reaction between NOx and NH3 on iron oxide-titanium oxide catalyst", *Journal of Physical Chemistry*, vol. 85, no. 26, pp. 4099–4102, 1981, ISSN: 00223654. DOI: 10.1021/j150626a029.

[17] H.-Y. Chen, "Cu/Zeolite SCR Catalysts for Automotive Diesel NOx Emission Control", in *Urea-SCR Technology for deNOx After Treatment of Diesel Exhausts*, I. Nova and E. Tronconi, Eds., 2014, ch. 5, pp. 123–147, ISBN: 9781489980700. DOI: 10.1007/978-1-4899-8071-7_5. [Online]. Available: http://link.springer.com/10.1007/978-1-4899-8071-7%7B%5C_%7D5.

[18] F. Gao and J. Szanyi, "On the hydrothermal stability of Cu/SSZ-13 SCR catalysts", *Applied Catalysis A: General*, vol. 560, no. April, pp. 185–194, 2018, ISSN: 0926860X. DOI: 10.1016/j.apcata.2018.04.040. [Online]. Available: https://doi.org/10.1016/j.apcata.2018.04.040.

[19] D. W. Fickel, E. D'Addio, J. A. Lauterbach, and R. F. Lobo, "The ammonia selective catalytic reduction activity of copper-exchanged small-pore zeolites", *Applied Catalysis B: Environmental*, vol. 102, no. 3-4, pp. 441–448, 2011, ISSN: 09263373. DOI: 10.1016/j.apcatb.2010.12.022. [Online]. Available: http://dx.doi.org/10.1016/j.apcatb.2010.12.022.

[20] S. I. Zones, "Zeolite SSZ-13 and Its Method of Preparation", *U S Patent*, no. 4544538A, pp. 4, 544, 538, 1985. [Online]. Available: https://patents.google.com/patent/US4544538A/en.

[21] International Zeolite Association, *CHA: Framework Type*. [Online]. Available: http://www.iza-structure.org/IZA-SC/framework.php?STC=CHA (visited on 09/13/2020).

[22] S. Zhang, L. Pang, Z. Chen, S. Ming, Y. Dong, Q. Liu, P. Liu, W. Cai, and T. Li, "Cu/SSZ-13 and Cu/SAPO-34 catalysts for deNOx in diesel exhaust: Current status, challenges, and future perspectives", *Applied Catalysis A: General*, vol. 607, no. August, p. 117 855, 2020, ISSN: 0926860X. DOI: 10.1016/j.apcata.2020.117855. [Online]. Available: https://doi.org/10.1016/j.apcata.2020.117855.

[23] U. Deka, A. Juhin, E. A. Eilertsen, H. Emerich, M. A. Green, S. T. Korhonen, B. M. Weckhuysen, and A. M. Beale, "Confirmation of isolated Cu 2+ ions in SSZ-13 zeolite as active sites in NH 3-selective catalytic reduction", *Journal of Physical Chemistry C*, vol. 116, no. 7, pp. 4809–4818, 2012, ISSN: 19327447. DOI: 10.1021/jp212450d.

[24] C. Paolucci, A. A. Parekh, I. Khurana, J. R. Di Iorio, H. Li, J. D. Albarracin Caballero, A. J. Shih, T. Anggara, W. N. Delgass, J. T. Miller, F. H. Ribeiro, R. Gounder, and W. F. Schneider, "Catalysis in a cage: Condition-dependent speciation and dynamics of exchanged cu cations in ssz-13 zeolites", *Journal of the American Chemical Society*, vol. 138, no. 18, pp. 6028–6048, 2016, ISSN: 15205126. DOI: 10.1021/jacs.6b02651.

[25] S. Li, H. Kong, and W. Zhang, "A Density Functional Theory Modeling on the Framework Stability of Al-Rich Cu-SSZ-13 Zeolite Modified by Metal Ions", *Industrial and Engineering Chemistry Research*, vol. 59, no. 13, pp. 5675–5685, 2020, ISSN: 15205045. DOI: 10.1021/acs.iecr.9b07082.

[26] C. W. Andersen, M. Bremholm, P. N. R. Vennestrøm, A. B. Blichfeld, L. F. Lundegaard, and B. B. Iversen, "Location of Cu2+ in CHA zeolite investigated by X-ray diffraction using the Rietveld/maximum entropy method", *IUCrJ*, vol. 1, pp. 382–386, 2014, ISSN: 20522525. DOI: 10.1107/S2052252514020181.

[27] F. Gao and C. H. Peden, "Recent progress in atomic-level understanding of Cu/SSZ-13 selective catalytic reduction catalysts", *Catalysts*, vol. 8, no. 4, 2018, ISSN: 20734344. DOI: 10.3390/catal8040140.

[28] Y. Cui, Y. Wang, E. D. Walter, J. Szanyi, Y. Wang, and F. Gao, "Influences of Na+ co-cation on the structure and performance of Cu/SSZ-13 selective catalytic reduction catalysts", *Catalysis Today*, vol. 339, no. February 2019, pp. 233–240, 2020, ISSN: 09205861. DOI: 10.1016/j.cattod.2019.02.037. [Online]. Available: https://doi.org/10.1016/j.cattod.2019.02.037.

[29] J. R. Di Iorio, S. Li, C. B. Jones, C. T. Nimlos, Y. Wang, E. Kunkes, V. Vattipalli, S. Prasad, A. Moini, W. F. Schneider, and R. Gounder, "Cooperative and Competitive Occlusion of Organic and Inorganic Structure-Directing Agents within Chabazite Zeolites Influences Their Aluminum Arrangement", *Journal of the American Chemical Society*, vol. 142, no. 10, pp. 4807–4819, 2020, ISSN: 15205126. DOI: 10.1021/jacs.9b13817.

[30] D. B. Williams and C. B. Carter, *Transmission Electron Microscopy*, 2. Boston, MA: Springer US, 2009, vol. 43, pp. 94–97, ISBN: 978-0-387-76500-6. DOI: 10.1007/978-0-387-76501-3. [Online]. Available: http://link.springer.com/10.1007/978-0-387-76501-3.

[31] P. Hartel, H. Rose, and C. Dinges, "Conditions and reasons for incoherent imaging in STEM", *Ultramicroscopy*, vol. 63, no. 2, pp. 93–114, 1996, ISSN: 03043991. DOI: 10.1016/0304-3991(96)00020-4.

[32] B. Fultz and J. Howe, *Transmission Electron Microscopy and Diffractometry of Materials*, ser. Graduate Texts in Physics. Berlin, Heidelberg: Springer Berlin Heidelberg, 2013, ISBN: 978-3-642-29760-1. DOI: 10.1007/978-3-642-29761-8. [Online]. Available: http://link.springer.com/10.1007/978-3-642-29761-8.

[33] S. J. Pennycook and P. D. Nellist, *Scanning Transmission Electron Microscopy*, S. J. Pennycook and P. D. Nellist, Eds. New York, NY: Springer New York, 2011, ISBN: 978-1-4419-7199-9. DOI: 10.1007/978-1-4419-7200-2. [Online]. Available: http://link.springer.com/10.1007/978-1-4419-7200-2.

[34] S. Pennycook, B. Rafferty, and P. Nellist, "Z-contrast Imaging in an Aberration-corrected Scanning Transmission Electron Microscope", *Microscopy and Microanalysis*, vol. 6, no. 4, pp. 343–352, 2000, ISSN: 1431-9276. DOI: 10.1007/s100050010045.

[35] H. Rose, "Correction of aperture aberrations in magnetic systems with threefold symmetry", *Nuclear Instruments and Methods in Physics Research*, vol. 187, no. 1, pp. 187–199, Aug. 1981, ISSN: 01675087. DOI: 10.1016/0029-554X(81)90488-2. [Online]. Available: https://linkinghub.elsevier.com/retrieve/pii/0029554X81904882.

[36] M. Haider, S. Uhlemann, E. Schwan, H. Rose, B. Kabius, and K. Urban, "Electron microscopy image enhanced", *Nature*, vol. 392, no. 6678, pp. 768–769, Apr. 1998, ISSN: 0028-0836. DOI: 10.1038/33823. [Online]. Available: http://www.nature.com/articles/33823.

[37] R. F. Egerton, "Radiation damage to organic and inorganic specimens in the TEM", *Micron*, vol. 119, no. November 2018, pp. 72–87, 2019, ISSN: 09684328. DOI: 10.1016/j.micron.2019.01.005.

[38] R. F. Egerton, P. Li, and M. Malac, "Radiation damage in the TEM and SEM", *Micron*, vol. 35, no. 6, pp. 399–409, 2004, ISSN: 09684328. DOI: 10.1016/j.micron.2004.02.003.

[39] A. Mayoral, P. A. Anderson, and I. Diaz, "Zeolites are no longer a challenge: Atomic resolution data by Aberration-corrected STEM", *Micron*, vol. 68, pp. 146–151, 2015, ISSN: 09684328. DOI: 10.1016/j.micron.2014.05.009.

[40] A. Mayoral, T. Carey, P. A. Anderson, and I. Diaz, "Atomic resolution analysis of porous solids: A detailed study of silver ion-exchanged zeolite A", *Microporous and Mesoporous Materials*, vol. 166, pp. 117–122, Jan. 2013, ISSN: 13871811. DOI: 10.1016/j.micromeso.2012.04.033. [Online]. Available: http://dx.doi.org/10.1016/j.micromeso.2012.04.033%20https://linkinghub.elsevier.com/retrieve/pii/S1387181112002466.

[41] A. Mayoral, T. Carey, P. A. Anderson, A. Lubk, and I. Diaz, "Atomic resolution analysis of silver ion-exchanged zeolite A", *Angewandte Chemie - Inter-*

national Edition, vol. 50, no. 47, pp. 11 230–11 233, 2011, ISSN: 14337851. DOI: 10.1002/anie.201105450.

[42] O. Ugurlu, J. Haus, A. A. Gunawan, M. G. Thomas, S. Maheshwari, M. Tsapatsis, and K. A. Mkhoyan, "Radiolysis to knock-on damage transition in zeolites under electron beam irradiation", *Physical Review B - Condensed Matter and Materials Physics*, vol. 83, no. 11, pp. 1–4, 2011, ISSN: 10980121. DOI: 10.1103/PhysRevB.83.113408.

[43] R. Csencsits and R. Gronsky, "Damage of zeolite Y in the TEM and its effects on TEM images", *Ultramicroscopy*, vol. 23, no. 3-4, pp. 421–431, 1987, ISSN: 03043991. DOI: 10.1016/0304-3991(87)90253-1.

[44] C. Li, Q. Zhang, and A. Mayoral, "Ten Years of Aberration Corrected Electron Microscopy for Ordered Nanoporous Materials", *ChemCatChem*, vol. 12, no. 5, pp. 1248–1269, 2020, ISSN: 18673899. DOI: 10.1002/cctc.201901861.

[45] T. Altantzis, E. Coutino-Gonzalez, W. Baekelant, G. T. Martinez, A. M. Abakumov, G. V. Tendeloo, M. B. Roeffaers, S. Bals, and J. Hofkens, "Direct Observation of Luminescent Silver Clusters Confined in Faujasite Zeolites", *ACS Nano*, vol. 10, no. 8, pp. 7604–7611, 2016, ISSN: 1936086X. DOI: 10.1021/acsnano.6b02834.

[46] C. Aydin, J. Lu, A. J. Liang, C. Y. Chen, N. D. Browning, and B. C. Gates, "Tracking iridium atoms with electron microscopy: First steps of metal nanocluster formation in one-dimensional zeolite channels", *Nano Letters*, vol. 11, no. 12, pp. 5537–5541, 2011, ISSN: 15306984. DOI: 10.1021/nl2034305.

[47] M. M. Treacy and J. M. Newsam, "Electron beam sensitivity of zeolite L", *Ultramicroscopy*, vol. 23, no. 3-4, pp. 411–419, 1987, ISSN: 03043991. DOI: 10.1016/0304-3991(87)90252-X.

[48] L. A. Bursill, J. M. Thomas, and K. J. Rao, "Stability of zeolites under electron irradiation and imaging of heavy cations in silicates", *Nature*, vol. 289, no. 5794, pp. 157–158, 1981, ISSN: 00280836. DOI: 10.1038/289157a0.

[49] L. A. Bursill, E. A. Lodge, and J. M. Thomas, "Zeolitic structures as revealed by high-resolution electron microscopy", *Nature*, vol. 286, no. 5769, pp. 111–113, Jul. 1980, ISSN: 0028-0836. DOI: 10.1038/286111a0. [Online]. Available: http://www.nature.com/articles/286111a0.

[50] *Format Specific Options (muSTEM) — ASE documentation*. [Online]. Available: https://wiki.fysik.dtu.dk/ase/ase/io/formatoptions.html%7B%5C#%7Dmustem (visited on 05/10/2021).

[51] L. Allen, A. D. Alfonso, and S. Findlay, *μSTEM*. 2018, pp. 1–30. [Online]. Available: https://github.com/HamishGBrown/MuSTEM.

[52] C. Koch, "Determination of Core Structure Periodicity and Point Defect Density Along Dislocations", *Dissertation*, no. May, 2002.

[53] A. Mayoral, J. G. Min, and S. B. Hong, "Aberration-corrected STEM analysis of the RHO family of zeolites with embedded isoreticular structures", *Microporous and Mesoporous Materials*, vol. 236, pp. 129–133, 2016, ISSN: 13871811. DOI: 10.1016/j.micromeso.2016.08.039.

[54] L. J. Allen, A. J. D'Alfonso, and S. D. Findlay, "Modelling the inelastic scattering of fast electrons", *Ultramicroscopy*, vol. 151, pp. 11–22, 2015, ISSN:

18792723. DOI: 10.1016/j.ultramic.2014.10.011. [Online]. Available: http://dx.doi.org/10.1016/j.ultramic.2014.10.011.

[55] J. M. Cowley and A. F. Moodie, "The scattering of electrons by atoms and crystals. I. A new theoretical approach", *Acta Crystallographica*, vol. 10, no. 10, pp. 609–619, 1957, ISSN: 0365-110X. DOI: 10.1107/s0365110x57002194.

[56] A. Hjorth Larsen, J. JØrgen Mortensen, J. Blomqvist, I. E. Castelli, R. Christensen, M. Dułak, J. Friis, M. N. Groves, B. Hammer, C. Hargus, E. D. Hermes, P. C. Jennings, P. Bjerre Jensen, J. Kermode, J. R. Kitchin, E. Leonhard Kolsbjerg, J. Kubal, K. Kaasbjerg, S. Lysgaard, J. Bergmann Maronsson, T. Maxson, T. Olsen, L. Pastewka, A. Peterson, C. Rostgaard, J. SchiØtz, O. Schütt, M. Strange, K. S. Thygesen, T. Vegge, L. Vilhelmsen, M. Walter, Z. Zeng, and K. W. Jacobsen, *The atomic simulation environment - A Python library for working with atoms*, Jun. 2017. DOI: 10.1088/1361-648X/aa680e.

[57] L. A. Passmore and C. J. Russo, *Specimen Preparation for High-Resolution Cryo-EM*, 1st ed. Elsevier Inc., 2016, vol. 579, pp. 51–86, ISBN: 9780128053829. DOI: 10.1016/bs.mie.2016.04.011. [Online]. Available: http://dx.doi.org/10.1016/bs.mie.2016.04.011.

[58] A. Wang, K. Lindgren, M. Di, D. Bernin, P. A. Carlsson, M. Thuvander, and L. Olsson, "Insight into hydrothermal aging effect on Pd sites over Pd/LTA and Pd/SSZ-13 as PNA and CO oxidation monolith catalysts", *Applied Catalysis B: Environmental*, vol. 278, no. May, 2020, ISSN: 09263373. DOI: 10.1016/j.apcatb.2020.119315.

[59] A. Mayoral, Q. Zhang, Y. Zhou, P. Chen, Y. Ma, T. Monji, P. Losch, W. Schmidt, F. Schüth, H. Hirao, J. Yu, and O. Terasaki, "Direct Atomic-Level Imaging of Zeolites: Oxygen, Sodium in Na-LTA and Iron in Fe-MFI", *Angewandte Chemie - International Edition*, pp. 2–10, 2020, ISSN: 15213773. DOI: 10.1002/anie.202006122.

[60] L. A. Bursill, E. A. Lodge, and J. M. Thomas, "Zeolitic structures as revealed by high-resolution electron microscopy", *Nature*, vol. 286, no. 5769, pp. 111–113, 1980, ISSN: 00280836. DOI: 10.1038/286111a0.

[61] L. Liu, M. Lopez-Haro, C. W. Lopes, C. Li, P. Concepcion, L. Simonelli, J. J. Calvino, and A. Corma, "Regioselective generation and reactivity control of subnanometric platinum clusters in zeolites for high-temperature catalysis", *Nature Materials*, vol. 18, no. 8, pp. 866–873, 2019, ISSN: 14764660. DOI: 10.1038/s41563-019-0412-6. [Online]. Available: http://dx.doi.org/10.1038/s41563-019-0412-6.

[62] N. Hiyoshi, T. Ikeda, Y. Hasegawa, and K. Sato, "Observation of La-exchanged NaY zeolite using aberration-corrected scanning transmission electron microscopy", *Microporous and Mesoporous Materials*, vol. 311, no. October 2020, p. 110 711, 2021, ISSN: 13871811. DOI: 10.1016/j.micromeso.2020.110711. [Online]. Available: https://doi.org/10.1016/j.micromeso.2020.110711.

[63] D. R. Mitchell and B. Schaffer, "Scripting-customised microscopy tools for Digital Micrograph™", *Ultramicroscopy*, vol. 103, no. 4, pp. 319–332, 2005, ISSN: 03043991. DOI: 10.1016/j.ultramic.2005.02.003.

[64] D. R. Mitchell, *HRTEM Filter*. [Online]. Available: http://www.dmscripting.com/hrtem%7B%5C_%7Dfilter.html (visited on 06/01/2021).

[65] M. M. Treacy and J. B. Higgins, "Collection of Simulated XRD Powder Patterns for Zeolites Fifth (5th) Revised Edition", *Collection of Simulated XRD Powder Patterns for Zeolites Fifth (5th) Revised Edition*, 2007. DOI: 10.1016/B978-0-444-53067-7.X5470-7.

[66] A. Mayoral, J. E. Readman, and P. A. Anderson, "Aberration-corrected STEM analysis of a cubic Cd array encapsulated in zeolite A", *Journal of Physical Chemistry C*, vol. 117, no. 46, pp. 24 485–24 489, 2013, ISSN: 19327447. DOI: 10.1021/jp409171q.

[67] J. A. Rice, "The Poisson Distribution", in *Mathematical Statistics and Data Analysis*, 3rd, Brooks/Cole, 2007, ch. 2.1.5, pp. 42–47, ISBN: 9780495118688.

A

Sample preparation parameters

Name	Amount of zeolite powder	Ethanol volume	Lacey or holey carbon	Time for sonication	Time to let solution settle	Number of drops applied	Plasma cleaned grid	Time in plasma cleaner	Type of sonicator
A	ca 7x7 mm	60 ml	L	30 min	5 min	3	yes	10s	Branson 3800
B	ca 3x3 mm	40 ml	L	30 min	15 min	1	yes	10s	Branson 3800
C	ca 3x3 mm	40 ml	L	30 min	30 min	1	yes	10s	Branson 3800
D	ca 3x3 mm	40 ml	L	30 min	40 min	1	yes	10s	Branson 3800
E	ca 1x1 mm	40 ml	L	30 min	1 h	1	yes	10s	Branson 3800
F	ca 1x1 mm	50 ml	L	30 min	1 h	1	yes	10s	Branson 3800
G	ca 2x2 mm	40 ml	L	30 min	40 min	4	yes	10s	Branson 3800
H	ca 2x2 mm	40 ml	L	30 min	40 min (+20 min)	8	yes	10s	Branson 3800
I	ca 2x2 mm	40 ml	L	30 min	70 min	4	yes	10s	Branson 3800
J	ca 4x4 mm	40 ml	L	45 min	40 min (+20 min)	5	yes	10s	Branson 3800

B

Error estimation

To estimate the variability of particle yield on each TEM grid during sample preparation it was assumed that the nanocrystal clusters spatially follow a Poisson distribution over the grid after they have been applied. This assumption holds if the particles are more or less evenly dispersed over the entire investigated area [67]. This was one of the reasons for limiting the analysis to a set number of central squares of the grid. Even if the application of multiple drops would form a dense ring of particles closer to the rim of the grid, we assume that the particles are still spread evenly in the innermost, central squares of the grid.

Five samples were created from two similar batches (G and G') using the same parameters as for the G'4 sample. The number of particles in the central four squares was counted and if any square was partially damaged, we extrapolated the particle density in the rest of the square over the damaged area. The error was defined as the standard deviation of the Poisson distribution (square root of the mean over the five samples) [67]. We finally assumed the error to be linearly proportional to the number of drops applied and extrapolated it to G'7 and G'10 in Fig. 4.4

Regarding the error estimation of the size distribution data, we assumed that each size category ($\geq$ 1 µm, 700-900 nm, 300-600 nm and 100-200 nm) followed their own Poisson distribution spatially over the central squares of the grid. Here we again calculated the standard deviation for each size category in the same manner as stated for particle yield above. We however assumed that the variation in size distribution is independent of the number of drops applied to the grid. Since the distribution results are presented in percent of total number of particles found (on the central four squares), we converted the standard deviations to percentage to get the errors in Fig. 4.5.

Discussion about error estimation

There is no apparent trend that could explain the low number of particles in sample G'7 compared to G'4 and G'10 in Fig. 4.4, except that the preparation method inherently has a large variance. The results of G'4 and G'10 are about 5 standard deviations away from the result of G'7, something which either would imply that G'7 is an extreme outlier or, more probably, that our error estimation fails to capture the true variance of the sample preparation. This could stem from a too small sample size or faulty assumptions, for example the assumption that errors are linearly proportional to the applied number of drops.

C

Aberration coefficients for Titan microscope

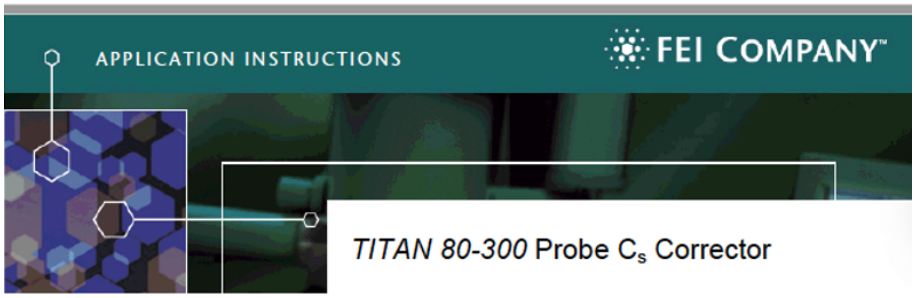

Table of aberration coefficients

The aberration coefficients are denoted by a single letter followed by a number. The number refers in each case to the order of the corresponding aberration coefficient, e.g., A2 stands for the 3fold astigmatism which is a second order aberration. The table below shows the tolerable aberrations to achieve a resolution of 0.14, 0.10 and 0.08 nm. The resolution as determined here is given by the (virtual) aperture size (values given in mrad) with a maximal phase shift of π/4.

Coefficient		Resolution 0.14 nm (13.8 mrad)	0.10 nm (19.7 mrad)	0.08 nm (24.6 mrad)	Control
C1	Defocus	3.2 nm	1.6 nm	0.8 nm	Adjustable[1]
Scherzer defocus		-35.4 nm	-17.7 nm	-8.5 nm	
A1	2fold astigmatism	3.2 nm	1.6 nm	0.8 nm	Adjustable[1]
A2	3fold astigmatism	345 nm	122 nm	41 nm	Adjustable
B2	Axial coma	120 nm	41 nm	14 nm	Adjustable
C3	Spherical aberration C_s	34 µm	8.3 µm	2.0 µm	Adjustable[2]
A3	4fold astigmatism	34 µm	8.3 µm	2.0 µm	Adjustable
S3	Star aberration	8.6 µm	2.1 µm	0.5 µm	Adjustable
A4	5fold astigmatism	3.1 mm	528 µm	89 µm	Adjustable
D4	Three lobe aberration	625 µm	106 µm	16.5 µm	Factory alinged
B4	Axial coma	625 µm	106 µm	16.5 µm	Factory alinged
C5	Spherical aberration	268 mm	32 mm	8.4 mm	Factory alinged
A5	6fold astigmatism	7.5 mm	836 µm	234 µm	Not adjustable

[1]Defocus and 2fold astigmatism are usually adjusted and fine tuned manually.
[2]If C3 (= C_S) is larger than ±50-70 µm, don't try adjust is with the software auto-alignment tool. Contact your FEI service engineer.

Limits for aberration coefficients: A detailed discussion of 'Residual wave aberrations' can be found in S. Uhlemann and M. Haider, Ultramicroscopy **72** (1998) 109-119. It also contains the definition of the aberration coefficients used by the software.

D

Simulations - Extended results

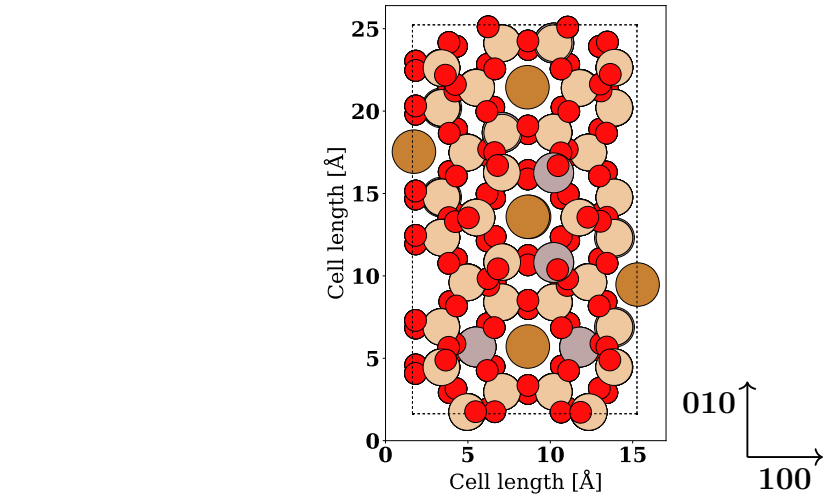

(a)

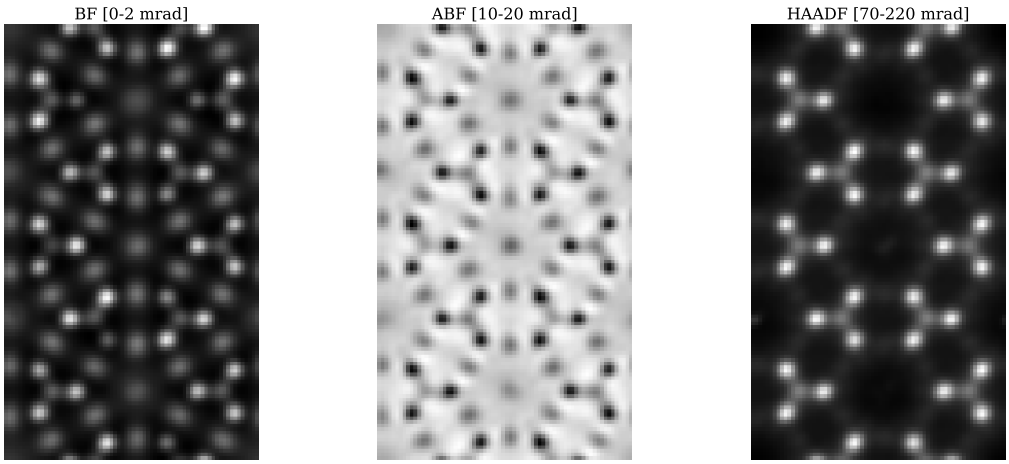

(b) (c) (d)

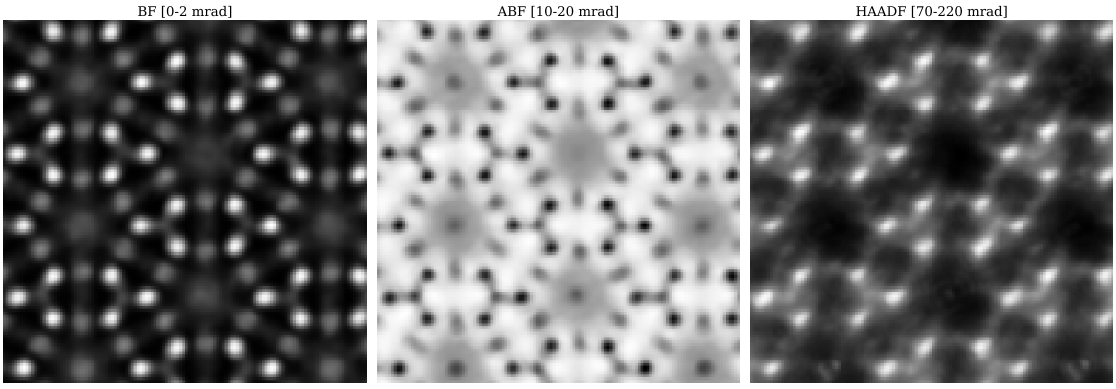

(e) (f) (g)

Figure D.1: Simulated high-resolution images along the [001]-direction with Cu dispersed among equal crystallographic 6MR sites. (a) Model cell. Light brown atoms are Si, brown atoms are Cu, red atoms are O and grey atoms are Al. (b-d) Images simulated in µSTEM using the absorptive model: (b) BF, (c) ABF and (d) HAADF. (e-g) Images simulated in QSTEM using the frozen phonon model: (e) BF, (f) ABF and (g) HAADF.

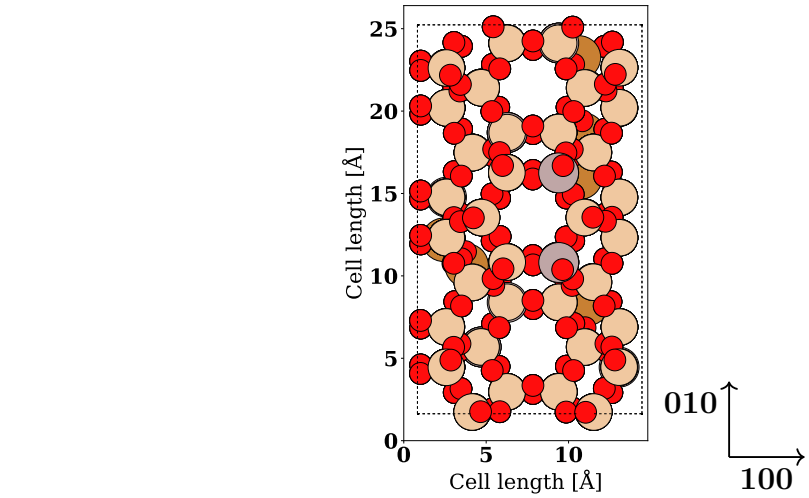

(a)

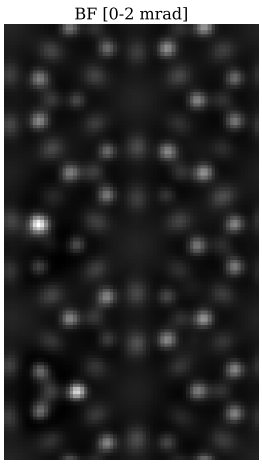

(b)

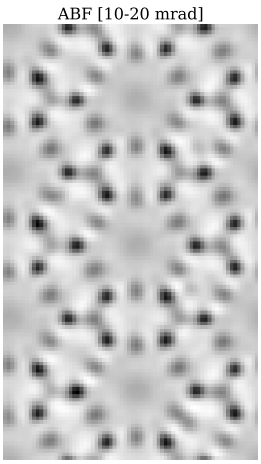

(c)

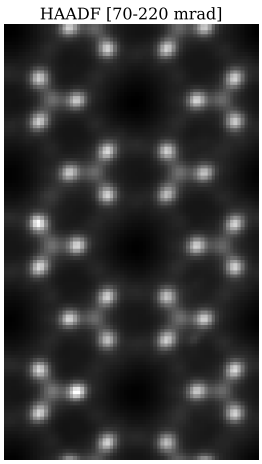

(d)

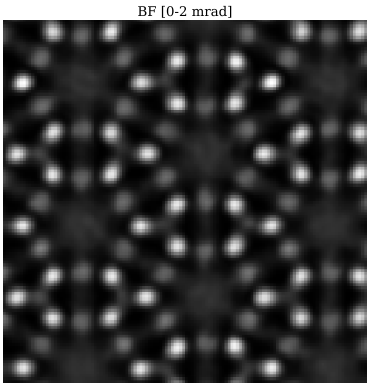

(e)

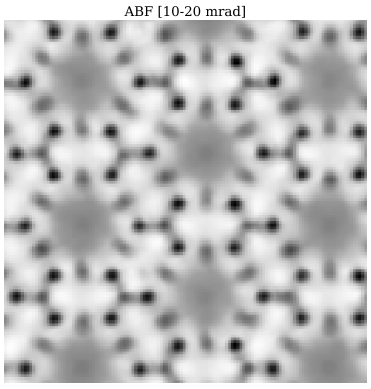

(f)

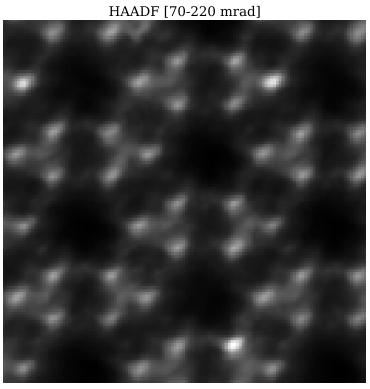

(g)

Figure D.2: Simulated high-resolution images along the [001]-direction with Cu dispersed among equal crystallographic 8MR sites. (a) Model cell. Light brown atoms are Si, brown atoms are Cu, red atoms are O and grey atoms are Al. (b-d) Images simulated in µSTEM using the absorptive model: (b) BF, (c) ABF and (d) HAADF. (e-g) Images simulated in QSTEM using the frozen phonon model: (e) BF, (f) ABF and (g) HAADF.

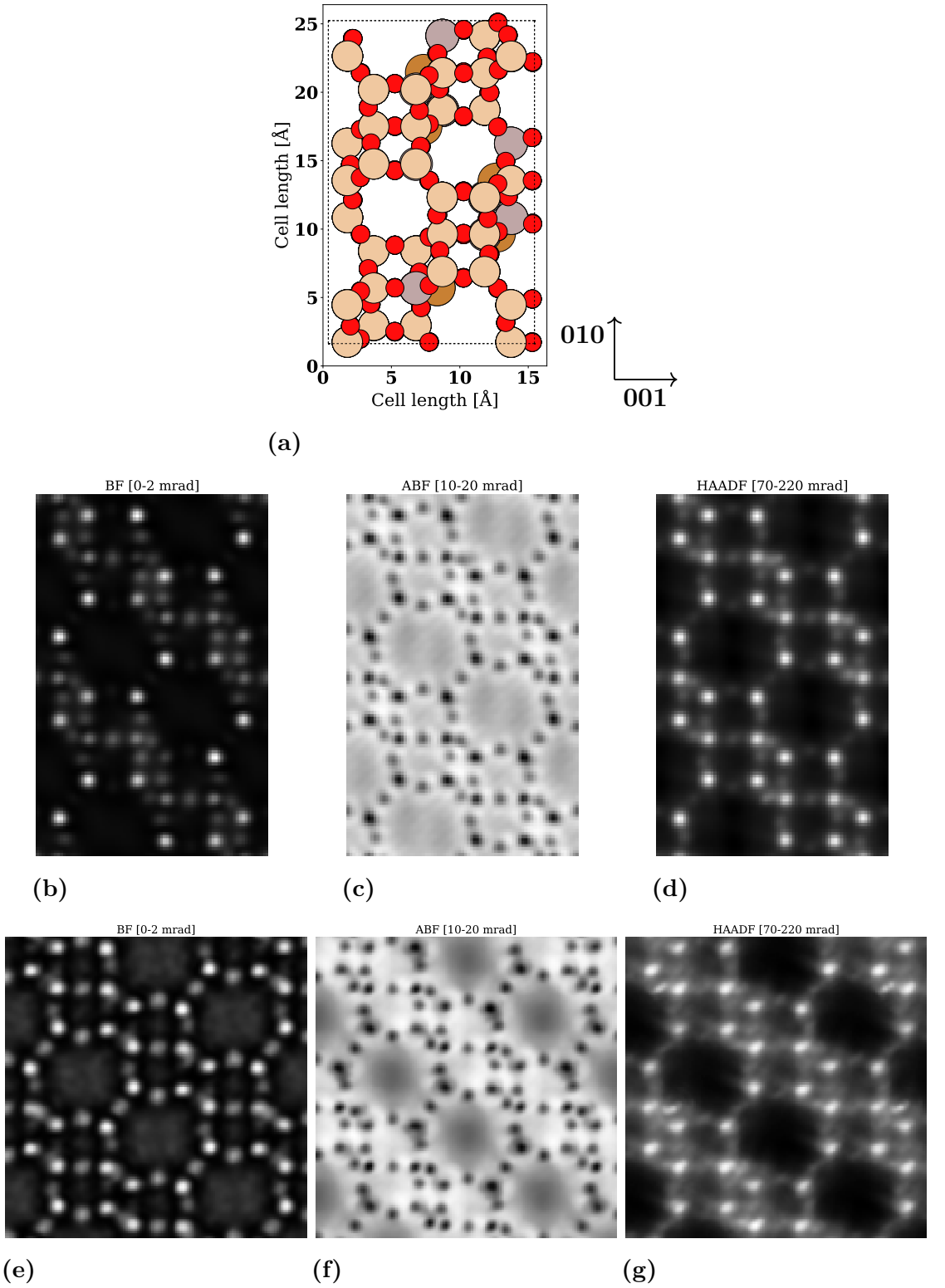

Figure D.3: Simulated high-resolution images along the [100]-direction with Cu dispersed among equal crystallographic 6MR sites. (a) Model cell. Light brown atoms are Si, brown atoms are Cu, red atoms are O and grey atoms are Al. (b-d) Images simulated in µSTEM using the absorptive model: (b) BF, (c) ABF and (d) HAADF. (e-g) Images simulated in QSTEM using the frozen phonon model: (e) BF, (f) ABF and (g) HAADF.

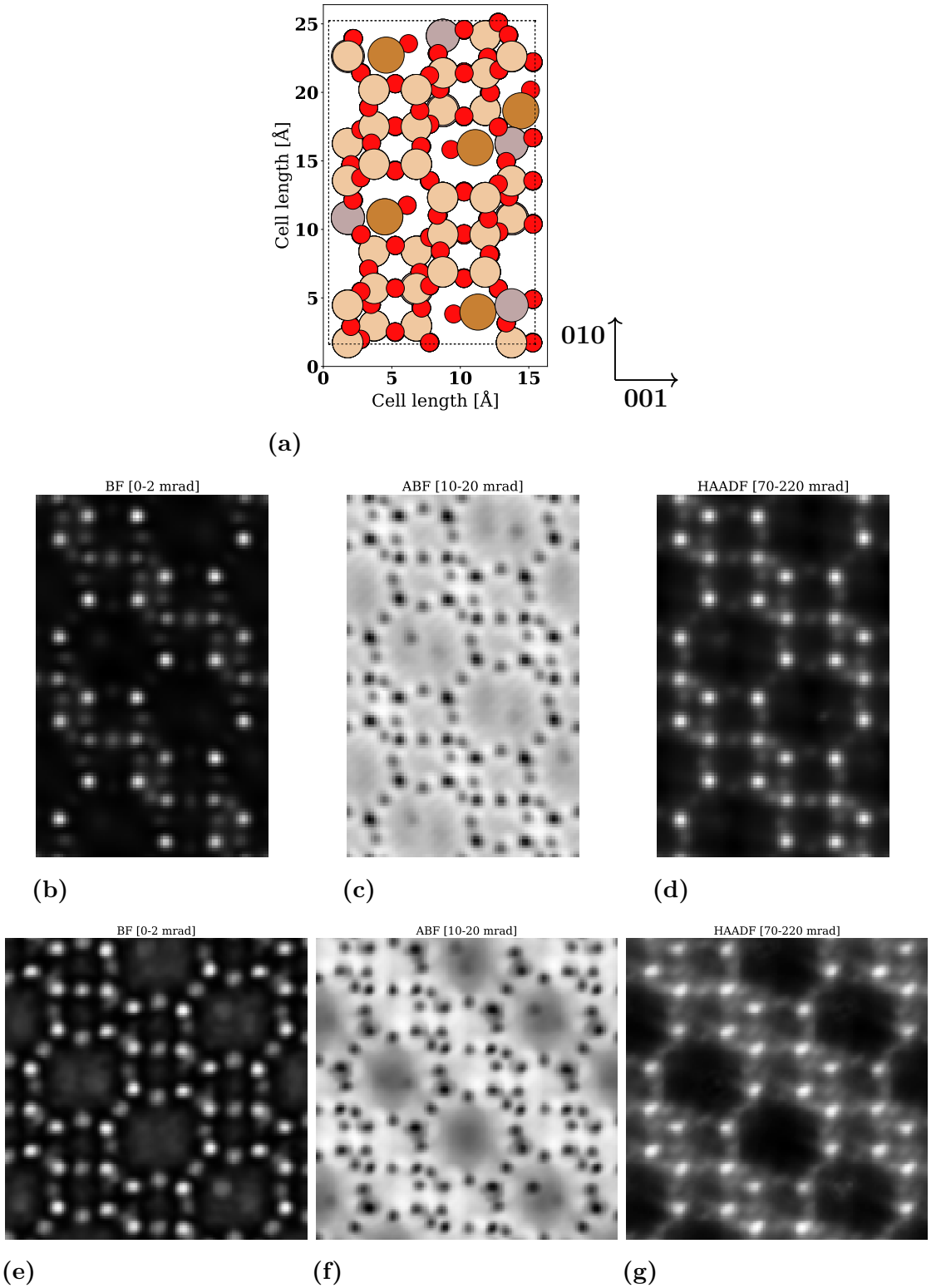

Figure D.4: Simulated high-resolution images along the [100]-direction with Cu dispersed among equal crystallographic 8MR sites. (a) Model cell. Light brown atoms are Si, brown atoms are Cu, red atoms are O and grey atoms are Al. (b-d) Images simulated in µSTEM using the absorptive model: (b) BF, (c) ABF and (d) HAADF. (e-g) Images simulated in QSTEM using the frozen phonon model: (e) BF, (f) ABF and (g) HAADF.